Inorganic Chemistry

pubs.acs.org/IC Article

Two Is Better than One? Investigating the Effect of Incorporating $Re(CO)_3Cl$ Side Chains into Pt(II) Diynes and Polyynes

Ashanul Haque, Rayya Al-Balushi, Idris Juma Al-Busaidi, Nawal K. Al-Rasbi, Sumayya Al-Bahri, Mohammed K. Al-Suti, Muhammad S. Khan,* Osama K. Abou-Zied,* Jonathan M. Skelton,* and Paul R. Raithby*

Cite This: *Inorg. Chem.* 2021, 60, 745−759 Read Online

ACCESS | Metrics & More | Article Recommendations | Supporting Information

ABSTRACT: Pt(II) diynes and polyynes incorporating 5,5′- and 6,6′-disubstituted 2,2′-bipyridines were prepared following conventional Sonogashira and Hagihara dehydrohalogenation reaction protocols. Using Pt(II) dimers and polymers as a rigid-rod backbone, four new heterobimetallic compounds incorporating $Re(CO)_3Cl$ as a pendant functionality in the 2,2′-bipyridine core were obtained. The new heterobimetallic Pt−Re compounds were characterized by analytical and spectroscopic techniques. The solid-state structures of a Re(I)-coordinated diterminal alkynyl ligand and a representative model compound were determined by single-crystal X-ray diffraction. Detailed photophysical characterization of the heterobimetallic Pt(II) diynes and polyynes was carried out. We find that the incorporation of the $Re(CO)_3Cl$ pendant functionality in the 2,2′-bipyridine-containing main-chain Pt(II) diynes and polyynes has a synergistic effect on the optical properties, red shifting the absorption profile and introducing strong long-wavelength absorptions. The Re(I) moiety also introduces strong emission into the monomeric Pt(II) diyne compounds, whereas this is suppressed in the polyynes. The extent of the synergy depends on the topology of the ligands. Computational modeling was performed to compare the energetic stabilities of the positional isomers and to understand the microscopic nature of the major optical transitions. We find that 5,5′-disubstituted 2,2′-bipyridine systems are better candidates in terms of yield, photophysical properties, and stability than their 6,6′-substituted counterparts. Overall, this work provides an additional synthetic route to control the photophysical properties of metallaynes for a variety of optoelectronic applications.

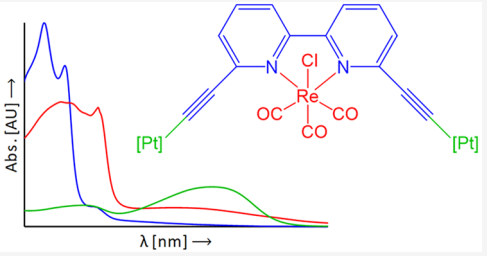

INTRODUCTION

Polyynes and poly(metallaynes) are widely studied materials with a diverse range of uses.[1] Enormous progress has been made in understanding the chemistry and photophysical properties of these materials, leading to a number of applications.[2−7] It is now well established that "rigid-rod" metalated systems offer improved properties and performance over their organic counterparts.[1,7,8] The inclusion of a transition metal ion such as Cr(III), Mo(II), W(III), Mn(I), Fe(II), Ru(II), Co(III), Rh(III), Ni(II), Pd(II), Pt(II), Au(I), *etc.* into the organic backbone through σ-linkages drastically modulates and often improves the structural, photophysical, and redox properties.[1,4] Insertion of a heavy metal ion into an organic backbone assists in bypassing spin-forbidden electronic transitions *via* intersystem crossing, leading to a substantial increase in the population of the emissive states and improved luminescence.[9] Based on this concept, several successful attempts have been made to combine the semiconducting properties of conjugated polyynes with the electronic effects induced by the presence of the heavy metal.[4,10−13] Many of these metallaynes have proven to be good candidates for applications in the areas of photovoltaics,[14] light-emitting diodes,[15] magnetic materials,[4] catalysts,[16] nonlinear optical materials,[17] molecular electronics,[1] bioimaging,[18] and the capture of organic and inorganic pollutants,[1] among others.

It is now well established that the optical properties of the poly(metallaynes) can be tuned by informed selection of the metals, spacers, and auxiliary ligands.[1,19] Several strategies are available to improve the properties of metallaynes, such as introducing donor−acceptor (D−A) ligands, increasing the effective conjugation length, changing the position of ligand attachment, shielding the polymer backbone, forming supramolecular assemblies, *etc.*[1] We recently demonstrated that Pt(II) diynes and polyynes bearing 2,7- and 3,6-carbazole spacers have differing levels of conjugation and frontier orbitals, leading to substantial variation in optical properties.[20] We have also shown that the topology around the metal centers has an impact on the isomerization of photoactive cores such as azobenzenes.[21]

Received: September 16, 2020
Published: December 31, 2020

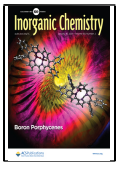

https://dx.doi.org/10.1021/acs.inorgchem.0c02747
Inorg. Chem. 2021, 60, 745−759

Scheme 1. Synthesis of the Precursors 1a−1c/2a−2c, the Pt(II) Diynes M1−M4, and the Pt(II) Polyynes P1−P4[a]

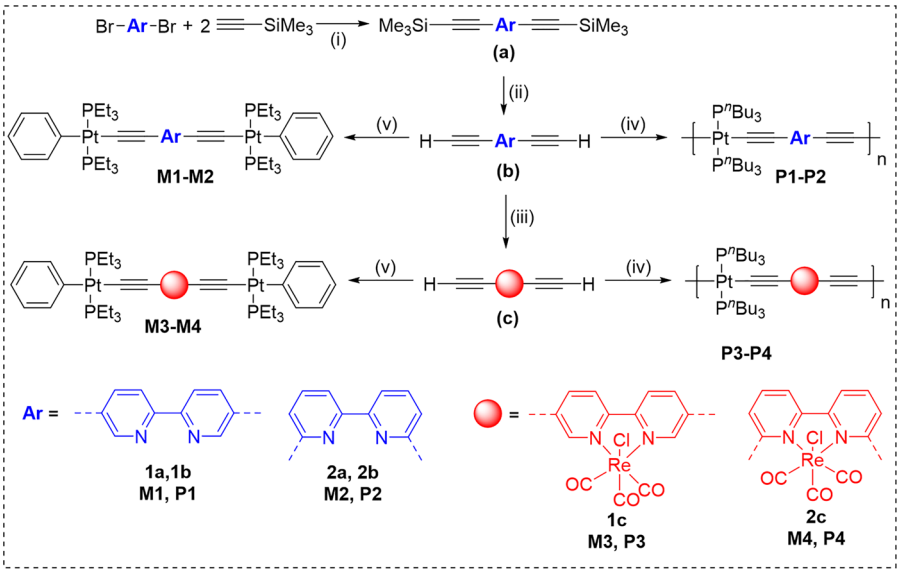

[a]Reaction conditions: (i) $Pd(OAc)_2$, CuI, PPh_3, $^iPr_2NH$/THF; (ii) KOH, MeOH/THF; (iii) $Re(CO)_5Cl$, toluene, 60 °C; (iv) 1.0 equiv of *trans*-$[(P^nBu_3)_2PtCl_2]$, CuI, $^iPr_2NH$, CH_2Cl_2; (v) 2.0 equiv of *trans*-$[Pt(PEt_3)_2PhCl]$, CuI, $^iPr_2NH$, CH_2Cl_2.

An additional and promising strategy to optimize the optoelectronic properties is to incorporate a second (hetero) metal ion into the main backbone or as a side chain.[22−25] The introduction of a second metal into a metallayne induces donor−acceptor interactions and influences the energy levels of the frontier orbitals[26] and hence the absorption/emission wavelength,[27] conductivity,[28] and redox behavior.[24,25] In particular, introduction of an ion such as Re(I) facilitates the movement of charges, narrows the band gap E_g, and produces long-lived luminescence.[29] It is reported that Re(I)-2,2′-diimine complexes show environment-sensitive metal-to-ligand charge-transfer (MLCT) excited states, which can be exploited to develop luminescent and redox-active materials.[29] Li and co-workers[24] found that the incorporation of Re(I) as a pendant side chain into a bithiazole-containing poly(platinayne) significantly modified the photophysical properties of the polymer. Such Pt(II)−Re(I) heterobimetallic systems are unique in allowing the effects of two different metal ions to be synergistically combined, potentially leading to new and useful physical properties.

Prompted by the exemplary features of Pt(II) diynes and polyynes and the interesting luminescence properties of the Re(I) fragment, we have synthesized and characterized two Re(I)-coordinated diterminal alkynyl ligands, *viz.*, $(CO)_3ClRe$-(I)-5,5′-bis(ethynyl)-2,2′-bipyridine (**1c**) and $(CO)_3ClRe$(I)-6,6′-bis(ethynyl)-2,2′-bipyridine (**2c**), together with the corresponding Pt(II) diynes **M3**/**M4** and polyynes **P3**/**P4**. Based on structural characterization, photophysical measurements, and computational modeling, we show how the incorporation of Re(I) influences the optical properties of the systems and thereby provides an additional dimension for modifying the properties of these conjugated metallopolymers.

RESULTS AND DISCUSSION

Synthesis and Spectroscopic Characterization. A modified Pd(II)/Cu(I)-catalyzed cross-coupling reaction between 5,5′- and 6,6′-dibromo-2,2′-bipyridine (Scheme 1) and ethynyltrimethylsilane (TMSA) was performed in $^iPr_2NH$/THF to obtain 5,5′-bis(trimethylsilylethynyl)-2,2′-bipyridine **1a** and 6,6′-bis(trimethylsilylethynyl)-2,2′-bipyridine **2a** (Scheme 1).[15] The diterminal alkynes 5,5′-bis(ethynyl)-2,2′-bipyridine **1b** and 6,6′-bis(ethynyl)-2,2′-bipyridine **2b** were then obtained by removal of the trimethylsilyl protecting groups with aqueous KOH in MeOH/THF. The diterminal alkynes were purified by silica gel column chromatography giving **1b** and **2b** in 60−76% yield. The protected and diterminal alkynes were fully characterized by infrared (IR) spectroscopy, multinuclear NMR spectroscopy, and electrospray ionization (ESI) mass spectrometry.[30,31]

The diterminal alkynes **1b** and **2b** were reacted with rhenium(I) pentacarbonyl chloride in toluene at 60 °C overnight under an argon atmosphere to obtain the Re-$(CO)_3Cl$-chelated 5,5′-bis(ethynyl)-2,2′-bipyridine **1c** and 6,6′-bis(ethynyl)-2,2′-bipyridine **2c** (Scheme 1). After purification by alumina column chromatography, the chelated diterminal alkynyl ligands were obtained in overall 49−62% yield and were again characterized using IR, multinuclear NMR, and mass spectrometry. The room temperature reaction of the $Re(CO)_3Cl$-incorporated diterminal alkynyl ligands **1c** and **2c** with 2 equiv of *trans*-$[Pt(PEt_3)_2(Ph)Cl]$ in $^iPr_2NH$/CH_2Cl_2 under an argon atmosphere in the presence of a CuI catalyst affords the Pt(II) diynes *trans*-$[(Et_3P)_2(Ph)Pt{-}C{\equiv}C{-}R{-}C{\equiv}C{-}Pt(Et_3P)_2(Ph)]$, with R = $(CO)_3ClRe$-2,2′-bipyridine-5,5′-diyl (**M3**) and R = $(CO)_3ClRe$-2,2′-bipyridine-6,6′-diyl (**M4**), as yellow solids in 40−45% yield (Scheme 1). Similarly, the CuI catalyzed dehydrohalogenation polycondensation reaction between *trans*-$[(P^nBu_3)_2PtCl_2]$ and **1c** and **2c** in a 1:1 ratio under similar reaction conditions readily affords the corresponding polyynes **P3**/**P4** (Scheme 1).

All compounds were readily soluble in CH_2Cl_2. The IR spectra of the Pt(II) diynes and polyynes show a single sharp $\nu_{C\equiv C}$ absorption around 2066−2089 cm^{-1}, consistent with a *trans* configuration of the alkynyl bridging ligands around the Pt(II) center. The carbonyl groups in the (bipy)Re(I)$(CO)_3Cl$ chromophore give rise to three clearly resolved IR bands in the range 1853−2018 cm^{-1} in a CH_2Cl_2 solution.[32] The presence

https://dx.doi.org/10.1021/acs.inorgchem.0c02747
Inorg. Chem. 2021, 60, 745−759

of the intact Re(I) chromophore in CH_2Cl_2 solutions of the polyynes **P3** and **P4** was confirmed from the presence of CO stretching bands between 1897 and 2018 cm^{-1} and 1871−2012 cm^{-1}, respectively. The Pt(II) di- and polyynes showed lower $\nu_{C\equiv C}$ frequencies than the corresponding chelated diterminal alkynyl ligands **1c** and **2c**, which we attributed to charge transfer between the metal and the 2,2′-bipyridine moiety.

The ^1H and ^{13}C NMR spectra of all compounds exhibit the expected signals including those from the acetylenic carbons (see the Experimental Section). The ^{31}P NMR spectra of the Pt(II) diynes and polyynes confirm the *trans* arrangement of the phosphine ligands, and the ^{31}P NMR spectra of **M3** and **M4** show larger $^1J_{Pt-P}$ coupling constants than the polyynes **P3** and **P4** by about 300 Hz.

Gel-permeation chromatography (GPC) using a polystyrene calibration gave molecular weights in the range of 90,000−100 000 g/mol for the polyynes **P1** and **P2**, corresponding to a degree of polymerization (DP) between 75 and 86 repeat units and a polydispersity index (PDI) between 1.3 and 1.7.[31] The weight-average molecular weights of **P3** and **P4** are in the range of 77,000−83 000 g/mol, corresponding to a DP between 50 and 55 and a PDI of 1.2−1.5. These molecular weights should, however, be treated with caution in view of the difficulties inherent in characterizing rigid-rod polymers with GPC. GPC does not give absolute molecular weights but provides a measure of the hydrodynamic volume, and rodlike polymers in a solution possess very different hydrodynamic properties to more flexible systems. Calibration of the GPC with a polystyrene standard is thus likely to overestimate the molecular weights of the polyynes. However, the lack of discernible resonances from end groups in the NMR spectra nonetheless points to a high degree of polymerization in these polyynes. ESI mass spectrometry confirmed the molecular structures of the alkynyl ligands and the dinuclear Pt(II)−Re(I) acetylide complexes.

X-ray Diffraction. To complement the spectroscopic characterization of the newly synthesized materials, we attempted to determine the crystal structures of the reported complexes by single-crystal X-ray diffraction.

Single crystals of the mononuclear Re complex **1c** were grown by slow diffusion of hexane into a solution of the complex in CH_2Cl_2. Crystallographic parameters for this structure are summarized in Table S1. **1c** crystallizes in the monoclinic space group $P2_1/n$. Figure 1a shows the molecular structure, and selected bond lengths and bond angles are given in Table 1. The crystal structure shows that the Re(I) center adopts a distorted octahedral coordination environment with three carbonyl groups, a chelating bipyridine ligand and one chlorido ligand. The structure also confirms the successful attachment of the acetylene R−C≡CH groups to the bipyridine ligand. The bipyridine ligands adopt a *cis* configuration, as defined by the N atoms, with an average Re−N(Py) bond distance of 2.192(9) Å. The three carbonyl ligands are in a facial (*fac*) configuration with C−Re−C bond angles in the range of 85.3(6)−90.5(5)°, and the average Re−CO bond length is 1.90(2) Å. The Re−Cl bond is longer at 2.468(3) Å, and the Cl_1−Re−C_{15} bond angle is 174.6(4)°. These parameters are comparable to those of previously published Re(I) bipyridine systems.[33] The crystal structure consists of vertical columns of stacked complexes stabilized by C−H···Cl (2.902 Å) and C−H···O−C (2.512 Å) intermolecular interactions, with horizontal π···Cl contacts (2.877 Å) between adjacent molecules (Figure 2a).

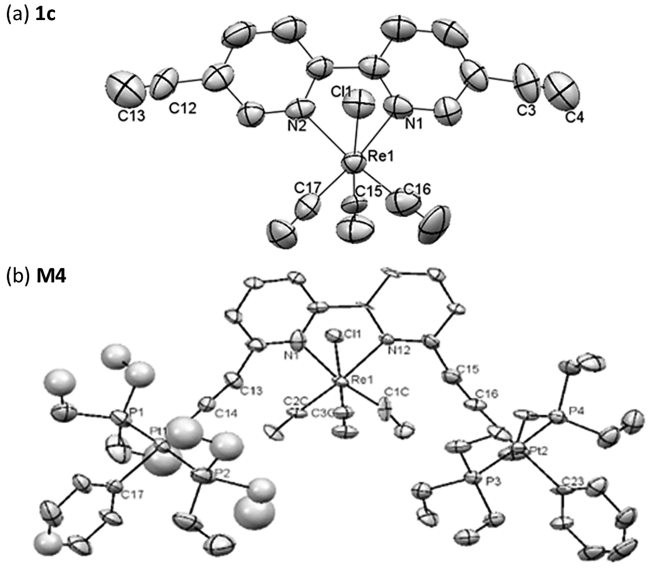

Figure 1. Crystal structures of (a) **1c** and (b) **M4** showing the atom-numbering scheme used in Table 1. The thermal ellipsoids are shown at 50% probability.

Attempts were also made to grow crystals of the $Re(CO)_3Cl$-incorporated model Pt(II) diyne compounds **M3** and **M4**. Single crystals of **M4** suitable for X-ray diffraction were grown by slow diffusion of hexane to a concentrated solution of the complex in CH_2Cl_2. Key crystallographic parameters for this structure are summarized in Table S1. Despite several attempts at doing so, we were not able to obtain crystals of **M3** that were suitable for single-crystal diffraction studies. Moreover, the crystals of **M4** were, in general, of poor quality and weakly diffracting, and thus while our structure is sufficient to confirm the overall molecular geometry, the bond parameters should be treated with caution.

M4 crystallizes in the triclinic space group *P*-1. The molecular structure comprises discrete trimetallic moieties defined by a central Re(2,2′-bipyridine-6,6′-diyl)$(CO)_3Cl$ unit attached to a pair of *trans*-[$(Ph)(PEt_3)_2Pt$−C≡C−] units (Figure 1b). The six-coordinate Re(I) metal center adopts a distorted octahedral geometry. In general, 2,2′-bipyridine derivatives of the *fac*-$Re(CO)_3Cl$ complex adopt an almost planar geometry with respect to the basal OC−Re−CO plane.[33] However, deviation from planarity can occur due to steric hindrance between functional groups on the 2,2′-bipyridine core and the carbonyl (CO) ligands on the metal, leading to changes in the properties of the spacer group. The two rings in the bipyridine spacer are slightly twisted with respect to one another, with a torsion angle of 13° defined by the N(1), C(6), C(7), and N(12) atoms. This hints at a degree of strain in the bipyridine ligand, and we anticipate that the deviation from planarity would lead to some disruption of the conjugation in the ligand π system compared to a more planar geometry.

Selected bond lengths and angles from the **M4** structure are summarized in Table 1. The Re−CO bond distances are in the range of 1.895(19)−1.911(18) Å, the average Re−N bond distance is 2.190(15) Å, and the Re−Cl bond distance is 2.514(4) Å. The N(1)−Re−N(12) bond angle is 76.4(6)°. The two Pt(II) centers adopt a distorted square planar

https://dx.doi.org/10.1021/acs.inorgchem.0c02747
Inorg. Chem. 2021, 60, 745−759

Table 1. Selected Bond Lengths (Å) and Bond Angles (deg) from the Crystal Structures of 1c and M4

distance	[Å]	angle	[deg]
		1c	
Re(1)−N(1)	2.189(8)	Re(1)−C(16)	1.877(19)
Re(1)−N(2)	2.194(9)	Re(1)−C(15)	1.908(17)
Re(1)−Cl(1)	2.468(3)	Re(1)−C(17)	1.923(13)
C(15)−Re(1)−N(1)	90.5(4)	C(16)−Re(1)−N(2)	173.7(5)
C(17)−Re(1)−N(1)	172.9(4)	C(15)−Re(1)−N(2)	94.9(4)
C(16)−Re(1)−C(17)	85.3(6)	C(17)−Re(1)−N(2)	98.4(4)
C(15)−Re(1)−C(17)	90.5(5)	N(1)−Re(1)−N(2)	74.5(4)
C(17)−Re(1)−Cl(1)	94.9(4)	C(15)−Re(1)−Cl(1)	174.6(4)
C(16)−Re(1)−N(1)	101.8(5)	C(16)−Re(1)−Cl(1)	90.2(5)
		M4	
Re(1)−C(3C)	1.895(19)	C(3C)−Re(1)−C(1C)	92.7(8)
Re(1)−C(1C)	1.91(2)	C(3C)−Re(1)−C(2C)	91.2(8)
Re(1)−C(2C)	1.911(18)	C(1C)−Re(1)−C(2C)	88.9(8)
Re(1)−N(1)	2.176(17)	C(3C)−Re(1)−N(1)	92.6(7)
Re(1)−N(12)	2.204(13)	C(1C)−Re(1)−N(1)	169.8(8)
Re(1)−Cl(1)	2.514(4)	C(2C)−Re(1)−N(1)	99.7(7)
Pt(1)−C(14)	2.008(17)	C(14)−Pt(1)−C(17)	176.6(10)
Pt(1)−C(17)	2.04(4)	C(14)−Pt(1)−P(2)	88.5(6)
Pt(1)−P(2)	2.280(7)	C(17)−Pt(1)−P(2)	90.2(6)
Pt(1)−P(1)	2.293(6)	C(14)−Pt(1)−P(1)	93.3(6)
Pt(2)−C(16)	2.003(18)	P(2)−Pt(1)−P(1)	175.8(3)
Pt(2)−C(23)	2.06(2)	C(16)−Pt(2)−C(23)	177.6(8)
Pt(2)−P(4)	2.281(5)	C(16)−Pt(2)−P(4)	87.4(5)
Pt(2)−P(3)	2.292(4)	C(23)−Pt(2)−P(4)	93.0(5)

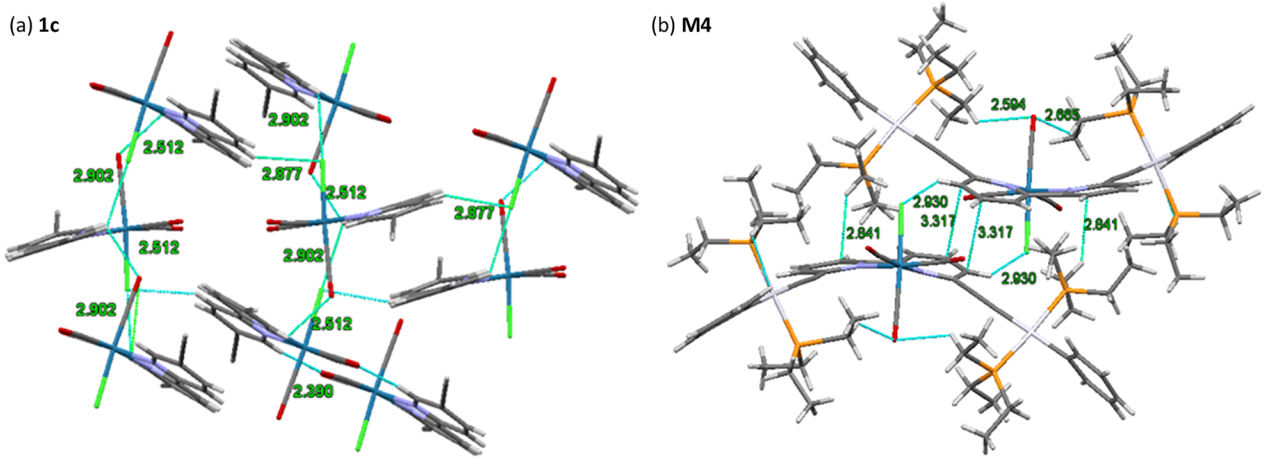

Figure 2. Crystal packing of **1c** (a), highlighting the intermolecular C−H···Cl, π···Cl, and C−H···O−C interactions, and of **M4** (b), highlighting the $\pi-\pi$ stacking and C−H···π/C−H···Cl interactions between adjacent pairs of molecules.

geometry. The Pt−C≡C bond distances are 2.008(17) and 2.003(18) Å for the Pt(1) and Pt(2) centers, respectively, which are consistent with related Pt(II) diyne complexes.[31,34] The Pt−P bond distances range from 2.280(7)−2.293(6) Å. The C−Pt−C angle is close to linear (176.6(10) and 177.6(8)° for Pt1 and Pt2, respectively). The presence of the Re(I) center and the *cis* configuration of the bipyridine rings of the spacer results in a Pt···Pt distance of 10.850 Å. Finally, the packing diagram of the complex (Figure 2b) shows a $\pi-\pi$ stacking interaction between the pyridine rings on adjacent pairs of molecules (3.317 Å separation between ring planes), together with evidence of C−H···π and C−H···Cl interactions.

Absorption Spectroscopy. Room temperature optical absorption spectra of the bis(ethynyl)bipyridine ligands **1b** and **2b**, Re(I)$(CO)_3$Cl-chelated ligands **1c** and **2c**, and the Re$(CO)_3$Cl incorporated Pt(II) di- and polyynes **M3**/**M4** and **P3**/**P4** were collected in 10^{-5} M CH_2Cl_2 solutions (Figure 3). Table 2 compares the absorption maxima of Pt(II) diynes and polyynes with and without the pendant Re(I) moieties, the latter taken from our previous work.[31] The absorption spectra of the ligands **1b**/**1c** and **2b**/**2c** are compared to those of the model compounds **M1**/**M2** and **M3**/**M4** in Figure S1.

The absorption spectra of the bis(ethynyl)-5,5′-bipyridine ligand **1b**, the Re$(CO)_3$Cl-chelated ligand **1c**, and the corresponding Pt(II) diyne **M3** and polyyne **P3** are compared in Figure 3a. The spectrum of **1b** displays intense absorption bands at $\lambda_{max} \approx 315$ and 328 nm and a shoulder feature around 348 nm. The spectrum of **1c** displays a noticeable shift in the absorption edge relative to **1b**, with absorption bands at $\lambda_{max} \approx$

https://dx.doi.org/10.1021/acs.inorgchem.0c02747
Inorg. Chem. 2021, 60, 745−759

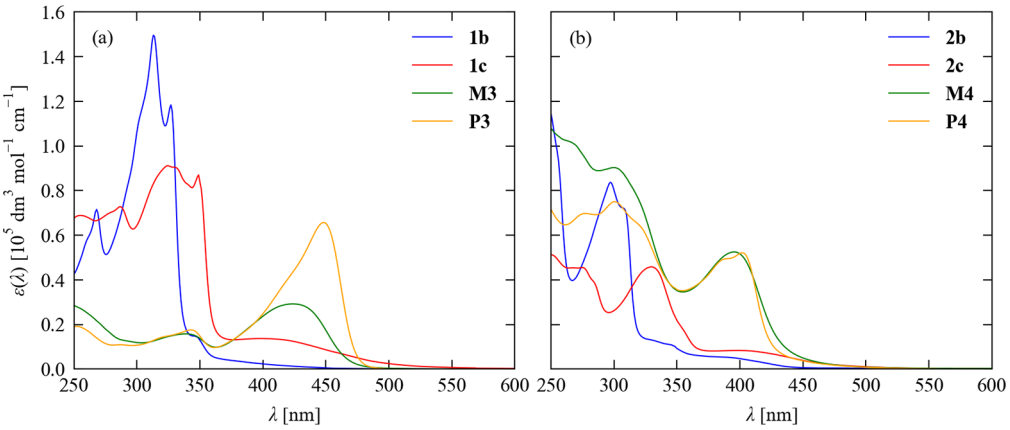

Figure 3. Comparison of the absorption spectra of the 5,5′-bis(ethynyl) bipyridine compounds **1b**, **1c**, **M3**, and **P3** (a) and the 6,6′-bis(ethynyl) bipyridine compounds **2b**, **2c**, **M4**, and **P4** (b). Both sets of spectra were measured in 10^{-5} M CH_2Cl_2 solutions at room temperature.

Table 2. Absorption Maxima of the Pt(II) Diynes and Polyynes with and without Pendant Re(I) Moieties Measured at Room Temperature[b]

without pendant Re(I) (ref 31)		with pendant Re(I) (this work)	
compd	λ_{max} [nm][a]	compd	λ_{max} [nm] ($\varepsilon \times 10^4$ dm^3 mol^{-1} cm^{-1})
M1	269, 297, 359, 381	**M3**	339 (1.58), 424 (2.92)
M2	258, 282, 298, 334, 349	**M4**	271 (9.94), 300 (9.03), 322 (7.28), 395 (5.25)
P1	271, 295, 362, 398	**P3**	343 (1.76), 419 (3.98), 448 (6.57)
P2	233, 264, 299, 337, 352	**P4**	276 (6.97), 300 (7.50), 324 (6.15), 388 (4.94), 402 (5.21)

[a] ε was not measured in the work in ref 31. [b] **M1**/**M2**, **P1**/**P2** - thin films; **M3**/**M4**, **P3**/**P4** - 10^{-5} M CH_2Cl_2 solution.

325, 332, and 350 nm. Absorption bands at ∼270 and 300−350 nm can be assigned to $\pi \rightarrow \pi^*$ transitions associated with the bipy/Ph and C≡C moieties, respectively, whereas broader bands at ∼400−450 nm can be attributed to MLCT transitions.[35] This is in line with previous studies that have identified low-lying MLCT excited states involving a Re dπ donor orbital and a ligand π^* acceptor,[36,37] with chelation to the metal serving to make the ligand a better electron acceptor and possibly also forcing it into a more planar conformation and increasing the effective conjugation in the ligand orbitals.[38] The MLCT state has been shown to be long-lived and to luminesce at longer wavelengths in the visible spectrum.[36,37,39] The extended tail of this ^{1}MLCT band is a signature of the extended electronic delocalization in the alkynyl bipyridine derivatives.[35] Clear effects of incorporating the Re(I) core into the Pt(II) diyne can be seen, for example, in the extended absorption of **1c** and **M3** relative to **1b** and **M1** (Figure 3, Figure S1). The steric hindrance due to the Pt(II) fragments is expected to be higher in systems based on 6,6′-bipyridine than in the 5,5′-counterparts, leading to different levels of conjugation. This is evidenced by the optical properties and computational modeling (*vide infra*), although ideally this should be confirmed by further structural characterization.

The Pt(II) diyne and polyyne systems **M3** and **P3** both display strong long-wavelength absorptions, with a broad band centered around $\lambda_{max} \approx 424$ in **M3** and an asymmetric feature in **P3** comprising a primary peak at $\lambda_{max} \approx 448$ nm and a secondary feature around 419 nm. Both also show weaker secondary maxima, which occur at ∼339 and 343 nm in **M3** and **P3**, respectively. There is thus a notable red shift in both bands and an enhancement of the extinction coefficient of the longer-wavelength bands on going from the diyne to the polyyne. Interestingly, calculations show that the long-wavelength transition in **M3** is not an MLCT band but is a bipyridine $\pi \rightarrow \pi^*$ transition that is highly red-shifted compared to **1b**/**1c** due to a destabilized highest occupied molecular orbital (HOMO, see below). While somewhat surprising, this does account for the large enhancement of the extinction coefficient compared to the long-wavelength MLCT band in **1c**.

The spectra of the 6,6′-bis(ethynyl)bipyridine complexes in Figure 3b illustrate that, as for the 5,5′-functionalized systems, chelation of the ligand to $Re(CO)_3Cl$ leads to a general red shift in the absorption profile and introduces an MLCT band, again at ∼410 nm. Incorporation of the chelated spacer unit into the Pt(II) diyne and polyyne results in a further red shift and an increase in extinction coefficient ($\lambda_{max} \approx 395$ and 388/402 nm, respectively). Comparison of the spectra of the heterometallic diynes and polyynes to the corresponding homometallic Pt(II) species (**M1**/**P1** and **M2**/**P2**) shows that adding a second metal ion leads to significant changes (Table 2), for example, a large bathochromic shift of the lower energy bands from 398 nm in **P1** to 448 nm in **P3**, which we ascribe to stabilization of the LUMO. The 6,6′-bipyridine species generally show blue-shifted absorption maxima compared to the corresponding 5,5′-bipyridine species, which we account for by the different positions of the alkynyl groups and the steric strain in the Pt(II) systems hindering the conjugation.

In principle, we might also expect the hindered conjugation in the 6,6′-bipyridine species to lead to lower extinction coefficients compared to the 5,5′-bipyridine analogues. While this is borne out for the **1b**/**2b** and **1c**/**2c** pairs, the **M3**/**M4** pair, and to some extent also **P3** and **P4**, shows the opposite trend. As shown in Figure 2b, the model complex **M4** exhibits molecular stacking in the solid state, and it is possible that aggregation in a solution through a similar mechanism may alter the extinction coefficient.[40] In particular, it has been reported that "V-shaped" conjugated molecules, such as **M4**,

https://dx.doi.org/10.1021/acs.inorgchem.0c02747
Inorg. Chem. 2021, 60, 745−759

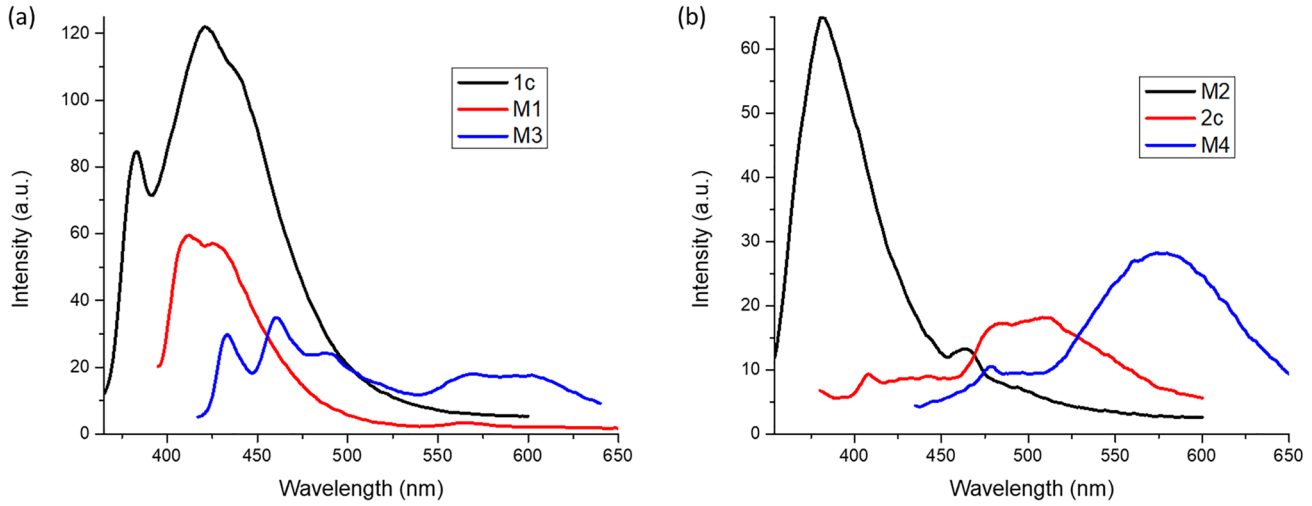

Figure 4. Room temperature emission spectra of (a) the 5,5′-bipyridine species **1c**, **M1**, and **M3** and (b) the corresponding 6,6′-bipyridine species **2c**, **M2**, and **M3**, measured in 3×10^{-5} M CH_2Cl_2 solutions.

Table 3. Excitation and Emission Wavelengths of the Bis(ethynyl)bipyridine Ligands 1c/2c and Model Compounds M1/M2 and M3/M4 Measured in 3×10^{-5} M CH_2Cl_2 Solutions and in the Solid State, Together with the Photoluminescence Quantum Yields Φ Measured in Solution

	solution (CH_2Cl_2)			solid state	
	λ_{ex} [nm]	λ_{em} [nm]	Φ[a]	λ_{ex} [nm]	λ_{em} [nm]
1c	350	382, 422	0.080	320	389, 695
2c	360	480, 514	0.13	320	388, 619
M1	390	414, 426, 565	not detected	390	423, 561, 608
M2	340	381, 466	not detected	340	371, 389, 693
M3	400	434, 462, 492, 568, 603	0.094	380	610, 656
M4	415	576	0.16	410	591

[a]The quantum yields are relative to coumarin 460, and the quantum yield of $Re(bpy)Cl(CO)_3$ is 0.0031 in CH_2Cl_2.[35]

form aggregates in halogenated solvents, leading to enhancement of the absorption cross section.[41] Measurement of the absorption spectra of **1c**/**2c**, **M1**/**M2**, and **M3**/**M4** at solution concentrations from 1×10^{-5} to 3×10^{-5} M (Figure S2) shows that although the band shape and λ_{max} remain the same, the molar extinction coefficient shows some sensitivity to the concentration. This suggests that the stacking and/or C−H···π/C−H···Cl interactions visible in the X-ray structure might influence the optical properties in solution. We also measured absorption and fluorescence emission spectra at varying concentrations (Figure S2) and found that increasing the concentration by up to 3× did not produce any major changes in spectral features, which is also in line with the results of the picosecond-nanosecond dynamics measurements presented below.

Photoluminescence Spectroscopy. Re(I) complexes are well-known for their intense, unstructured emission in the orange region of the visible spectrum, which originates from ^{3}MLCT excited states.[42] The energy, the intensity, and the lifetime of the emission are highly sensitive to the nature of the diimine and ancillary ligands,[43] and a large range of photoluminescence quantum yields (PLQYs) has been reported for Re(I) complexes.[42] The linkage of two metal atoms to the same chromophore has been shown to increase the metal *d* character in the frontier molecular orbitals, thereby enhancing the spin−orbit coupling between the emissive triplet state and the singlet manifold.[44] Linking two heavy metals to a single heterocyclic ligand is thus an interesting potential strategy for improving the PL properties of neutral Re(I) complexes.

Room temperature emission spectra of the Re(I)-coordinated ligands **1c**/**2c**, the homometallic Pt(II) diynes **M1**/**M2**, and the heterobimetallic Pt(II)−Re(I) diynes **M3**/**M4** were collected in 3×10^{-5} M CH_2Cl_2 solutions (Figure 4, Table 3). We also collected room-temperature solid-state emission spectra of the compounds (Figure S3), together with fluorescence excitation and emission spectra in CH_2Cl_2 solutions (Figure S4). The spectra are somewhat complex and composed of multiple maxima and/or shoulder features. The fluorescence excitation spectra of **2c**, **M1**, **M2**, and **M4** are similar to the absorption spectra, providing evidence that the measured emission is from the metal complexes, whereas those of **1c** and **M3** show a significant red shift, which we tentatively ascribe to solution effects such as aggregation or ligand dissociation (Figure S4).

As is commonly observed in Re(I) acetylide complexes, the Re(I)-chelated bipyridine ligands **1c**/**2c** and the bimetallic diyne model complexes **M3**/**M4** were all found to be emissive at room temperature both in a solution and in the solid state. The solution spectra of all four compounds show a strong primary luminescence feature and several weaker bands at longer wavelengths. Upon excitation at 390 and 340 nm, the Pt(II) diynes **M1** and **M2** also show emission in solution from ∼380−565 nm. The emission profiles were found to be red-shifted in the solid state (Table 3).

https://dx.doi.org/10.1021/acs.inorgchem.0c02747
Inorg. Chem. 2021, 60, 745−759

Table 4. Parameters for the Fits in Figure 5 Listing the Excited-State Lifetime Components τ_n (n = 2−3) and Their Corresponding Contributions α_n to the Overall Decay Transients

	λ_{ex} [nm]	λ_{det} [nm]	τ_1 [ps]	α_1	τ_2 [ns]	α_2	τ_3 [ns]	α_3
1c	350	420	684 ± 51	0.75	2.43 ± 0.09	0.25		
2c	350	500	597 ± 55	0.61	2.74 ± 0.16	0.34	20−23[a]	0.05
M3	380	580	200 ± 30	0.79	3.14 ± 0.22	0.20	20−23[a]	0.01
M4	380	580	359 ± 51	0.38	5.66 ± 0.38	0.21	22.2 ± 0.7	0.41

[a]Large uncertainty due to small contribution.

At room temperature, the photoluminescence quantum yield Φ (PLQY; Table 3) of **M1** and **M2** was very low and could not be reliably measured. From computational modeling studies (see below), the lowest-lying excited states of these compounds are $\pi \rightarrow \pi^*$ transitions, which are usually nonemissive at ambient temperature. On the other hand, excitation of heterobimetallic complexes **M3** and **M4** at 400 and 415 nm in a solution, and 380 and 410 nm in the solid state, led to strong emission in the yellow-orange region of the spectrum as expected for diimine Re(I) tricarbonyl species. We ascribe the shorter-wavelength emission to the reverse of the Re $d\pi \rightarrow$ bipyridine π^* MLCT transition as reported for other Re(I) chromophores.[29] While we were not able to assign the longer-wavelength transitions definitively, quantum-chemical calculations (see below) suggest that they may be associated with emission from formally spin-forbidden triplet states. The PLQY measured for the heterobimetallic complexes is also higher than for Re(bpy)Cl(CO)$_3$ (3.1×10^{-3} in CH_2Cl_2),[35] which indicates that the incorporation of a second metal limits nonradiative decay pathways. In general, our data indicates that incorporation of the Re(I) fragment into the heterobimetallic diynes improves the PLQY and leads to a red shift of emission maxima, although the emission intensity from the heterobimetallic complexes is lower than that from the homometallic Re(I) complexes at shorter wavelengths. As expected, the emission properties of the 5,5′- and 6,6′-systems differ significantly, which can be attributed to geometric constraints limiting the conjugation between the bipyridine and Pt(II) cores separated by the ethynyl units.

In contrast to the solution spectra, the position of the band centers in the solid-state spectra of **1c** and **2c** is very similar (Figure S3). The emission profiles of the model compounds **M3** and **M4** are both red-shifted compared to the chelated spacers, and the shift in emission wavelength of **M3** is more prominent than that of **M4**. Finally, in contrast to **M3** and **M4**, the polymers **P3** and **P4** were found to exhibit only weak emission both in solution and in the solid state at room temperature (Figure S5). The same was found for **P1** and **P2**.[31] The solution emission profiles of **P3** and **P4** are very similar to those of 5,5′-dibromobipyridine and 6,6′-dibromoipyridine, respectively, suggesting a dominant bipyridine-centered emission and suppression of the reverse MLCT transition seen in the chelated spacers **1c**/**2c** and the model compounds **M3**/**M4**.

Picosecond-Nanosecond Dynamics. Time-resolved fluorescence spectra of **1c**, **2c**, **M3**, and **M4** in CH_2Cl_2 were measured at room temperature close to the emission maxima in Table 3. The transients are shown in Figure 5, and parameters from a series of multiexponential fits are summarized in Table 4. Decay transients measured over a longer observation window, in order to accurately characterize longer-lived components, are shown in Figure S6.

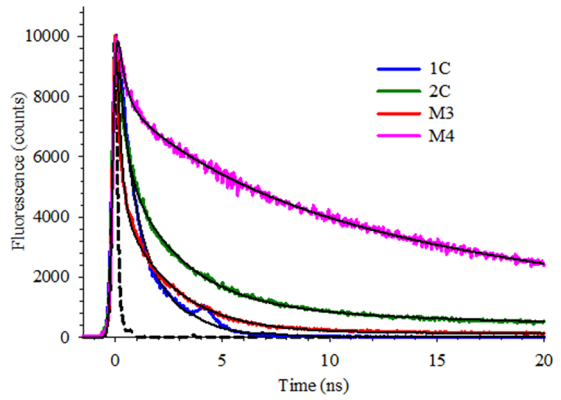

Figure 5. Room temperature fluorescence decay transients of **1c**/**2c** and **M3**/**M4** in CH_2Cl_2 (1×10^{-5} M). The instrument response function (IRF) is shown as a dashed black line. The black solid lines show fits of the measured transients to multiexponential functions. The excitation and detection wavelengths and the fit parameters are given in Table 4. Note that the artifact at ∼4 ns in the **1c** decay transient is due to "afterpulsing" in the photomultiplier tube detector and is excluded from the fitting, so it does not affect the values reported in Table 4.

Two components with lifetimes τ = 684 ps and 2.43 ns were obtained for **1c**. The shorter-lived component can be assigned to the relaxation of the MLCT state, whereas the nanosecond lifetime of the other component is typical of $\pi \rightarrow \pi^*$ decay and can thus be ascribed to the bipyridine ligand. In **2c**, the 6,6′ substitution pattern reduces the lifetime of the MLCT state to 597 ps compared to the 5,5′-substituted **1c** but raises the lifetime of the π^* decay to 2.74 ns and introduces a new, long-lived state with a lifetime of 20−23 ns. The latter are indicative of improved conjugation increasing the local heterogeneity of the system.

The presence of the Pt(II) fragments in **M3** further reduces the lifetime of the MLCT state to 200 ps but slightly increases the π^* lifetime to 3.14 ns. This can be accounted for through increased stability of the π^* state due to the more extended conjugation in the planar structure. **M3** also exhibits a very small contribution from the longer-lived component (20−23 ns) seen in **2c**. In **M4**, the steric effects due to the Pt(II) fragments in the 6,6′ positions lead to an increased contribution from the long-lived state (20−23 ns) at the expense of the MLCT state, as indicated by the fitting weights in Table 4. These effects also increase the π^* lifetime to 5.66 ns.

Increasing the concentration of the four species from 1×10^{-5} to 3×10^{-5} M did not produce any notable changes to the measured fluorescence decay transients (Figure S7). This indicates that increasing the concentration does not lead to excimer formation, as this would typically cause a buildup of signal (rise time) in the transients similar to that found in other systems such as pyrenes.[45] The increase in concentration may,

https://dx.doi.org/10.1021/acs.inorgchem.0c02747
Inorg. Chem. 2021, 60, 745−759

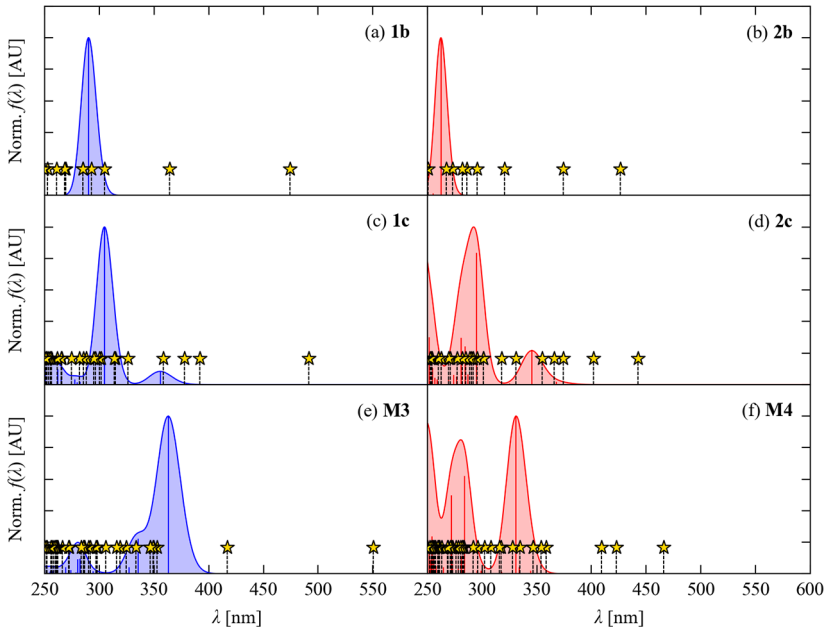

Figure 6. Simulated optical absorption spectra of the bis(ethynyl) bipyridine ligands **1b** and **2b** (a, b), $Re(CO)_3Cl$-chelated ligands **1c** and **2c** (c, d), and Pt(II) diynes **M3** and **M4** (e, f) obtained from time-dependent density-functional theory (TD-DFT) with an implicit CH_2Cl_2 solvent. In each subplot, the simulated spectra (blue/red shaded regions) are generated from the singlet (spin-allowed) excitations as a sum of Gaussian functions with a nominal line width σ of 0.1 eV. The wavelengths and relative oscillator strengths of individual transitions are marked by solid vertical lines of the same color as the spectrum. The wavelengths of triplet (forbidden) transitions are shown as dashed vertical lines and gold stars.

however, still lead to aggregation in the ground state, which explains the increase in the extinction coefficient observed in the absorption spectroscopy measurements.

Computational Modeling. To better understand the changes in optical properties on chelating the bipyridine units to the Re(I) centers and subsequently incorporating the chelated spacers into the Pt(II) model complexes, we carried out molecular quantum-chemical calculations using density-functional theory (DFT) on the bipyridine-based diterminal alkynyl ligands **1b** and **2b**, chelated diterminal alkynyl ligands **1c** and **2c**, and the Pt(II) diynes **M3** and **M4**. To match the conditions of the solution measurements as closely as possible, the calculations were performed with an implicit solvent of CH_2Cl_2.

Images of the optimized structures are given in Figures S8–S13, and the Cartesian coordinates are provided in Listings S1–S6. For all three pairs, we found that the 5,5′-bis(acetylide) bipyridine compounds were more energetically favorable (in CH_2Cl_2) than the 6,6′-analogues, with **1b**, **1c**, and **M3** calculated to be 7.44, 30.3, and 7.97 kJ mol^{-1} lower in energy than the corresponding **2b**, **2c**, and **M4** compounds, respectively.

Simulated optical absorption spectra obtained using time-dependent DFT (TD-DFT; Figure 6) reproduce the key trends in the measured spectra in Figure 3. For both bipyridine ligands, the calculations predict a red shift in the absorption profile and the appearance of new longer-wavelength absorption bands upon chelation with $Re(CO)_3Cl$, followed by a further red shift and enhancement of the oscillator strengths of the long-wavelength bands on incorporation of the chelated spacer units into Pt(II) diynes. Bearing in mind the use of a uniform line width when simulating the spectra and the fact that we only calculated the lowest-lying excited states of the larger complexes, the positions and intensities of the bands in the simulated spectra are a reasonable qualitative match to the measured absorption profiles.

The calculations also predict that all six compounds possess low-lying triplet (spin-forbidden) excited states 100–150 nm below the onset of the absorption from the lowest-energy singlet states (marked by stars and dashed lines in Figure 6). The density of these triplet states generally increases on going from the spacer ligands **1b**/**2b** to the chelated spacers **1c**/**2c** to the model compounds **M3**/**M4**. As noted in the previous section, these states may be associated with the weaker long-wavelength features in the solution emission spectra in Figure 4. Although it is, in principle, possible to model emission processes using TD-DFT, the procedure is considerably more involved than calculating the transition wavelengths and oscillator strengths to model absorption spectra, and we do not consider it feasible to do so for the six compounds being examined in this work.

The brightest singlet (spin-allowed) transitions and the 2–3 lowest-lying triplet (spin-forbidden) transitions in the simulated spectra in Figure 6 were analyzed by inspecting the molecular orbitals involved and, for transitions comprising more than one significant excitation between occupied and virtual states, by using the method of natural transition orbitals (NTOs) to visualize the composite occupied "particle" and unoccupied "hole" states.[41] Table 5 lists the calculated wavelengths, oscillator strengths, and our assignments of the brightest singlet (spin-allowed) transitions in each of the six complexes, while Table 6 lists the wavelengths and the assignments of the low-lying triplet (spin-forbidden) states. A full breakdown of the states listed in Tables 5 and 6 into transitions between pairs of occupied and virtual orbitals, and isosurfaces showing the NTOs, is given in Tables S2–S13 and Figures S14–S27/S31–S47, respectively.

A comparison of the oscillator strengths of the spin-allowed transitions in the 5,5′-bis(acetylide) bipyridine compounds to

https://dx.doi.org/10.1021/acs.inorgchem.0c02747
Inorg. Chem. 2021, 60, 745–759

Table 5. Transition Wavelengths λ, Oscillator Strengths f, and Assignments of the Brightest Singlet (Spin-Allowed) Transitions in the Bipyridine Spacers 1b/2b, Re(CO)$_3$Cl-Chelated Bipyridine Spacers 1c/2c, and Model Pt-Incorporated Diyne Compounds M3/M4

λ [nm]	f	assignment	λ [nm]	f	assignment
	1b			**2b**	
290	1.294	$\pi \rightarrow \pi^*$	262	0.566	$\pi \rightarrow \pi^*$
	1c			**2c**	
355	0.078	MLCT	345	0.066	MLCT
305	0.937	$\pi \rightarrow \pi^*$	295	0.256	dominant $\pi \rightarrow \pi^*$
			284	0.073	dominant MLCT
			280	0.090	dominant MLCT
	M3			**M4**	
363	1.635	$\pi \rightarrow \pi^*$ + MLCT (Pt)	331	0.595	$\pi \rightarrow \pi^*$ + MLCT (Pt)
335	0.356	MLCT (Re)	284	0.368	mixed
327	0.063	MLCT (Re)	281	0.063	mixed

Table 6. Transition Wavelengths λ and Assignments of the Low-Lying Triplet (Spin-Forbidden) Transitions in the Bipyridine Spacers 1b/2b, Re(CO)$_3$Cl-Chelated Bipyridine Spacers 1c/2c, and Model Pt-Incorporated Diyne Compounds M3/M4

λ [nm]	assignment	λ [nm]	assignment
	1b		**2b**
474	$\pi \rightarrow \pi^*$	426	$\pi \rightarrow \pi^*$
364	$\pi \rightarrow \pi^*$	374	$\pi \rightarrow \pi^*$
305	$\pi \rightarrow \pi^*$	320	$\pi \rightarrow \pi^*$
	1c		**2c**
492	$\pi \rightarrow \pi^*$	443	mixed
391	dominant MLCT	402	mixed
377	MLCT	374	dominant MLCT
	M3		**M4**
550	$\pi \rightarrow \pi^*$	466	dominant $\pi \rightarrow \pi^*$
417	$\pi \rightarrow \pi^*$	423	dominant $\pi \rightarrow \pi^*$
		409	$\pi \rightarrow \pi^*$

those of the 6,6′-bipyridine analogues shows that the latter are, in general, significantly weaker. The simulated spectrum of the (bisethynyl)bipyridine ligand **1b** (Figure 6a) shows a single prominent peak at 290 nm corresponding to the $\pi \rightarrow \pi^*$ electronic transition between the highest-occupied and lowest-unoccupied molecular orbitals (HOMO/LUMO; Figure 7a). The lowest-energy transition in the 6,6′-bis(ethynyl)bipyridine analogue **2b** occurs at a shorter wavelength of 262 nm and has a much lower oscillator strength of f = 0.57 vs 1.29 (Figure 6b). As in **1b**, the major component of the transition is the HOMO → LUMO excitation, but there is a substantial minor component associated with the HOMO → LUMO+2 excitation (Figure 7b). Comparison of the LUMOs of **1b** and **2b** shows that the different substitution pattern in **2b** lowers the degree of conjugation in the LUMO, and comparison of the orbital energies in **1b** and **2b** (Figure S28) indicates that the higher energy (shorter wavelength) transition in **2b** is most likely due to destabilization of the LUMO. The lower degree of conjugation also leads to poorer spatial overlap with the HOMO, which explains the mixing of the LUMO+2 orbital into the $\pi \rightarrow \pi^*$ excited state. This would further raise the transition energy, and the poorer spatial overlap between the HOMO and LUMO may explain the lower oscillator strength of the transition compared to the 5,5′-bipyridine analogue **1b**.

Chelation of **1b** results in new frontier Re-based orbitals, of which the HOMO - 1 orbital has the best spatial overlap with the bipyridine-based LUMO and gives rise to a weak MLCT band at 355 nm (Figure 6c). The HOMO - 3 orbital remains similar in form to the HOMO in **1b**, and the much stronger $\pi \rightarrow \pi^*$ transition occurs at 305 nm. The particle and hole states obtained from the NTO analysis of the two transitions are shown in Figure 8. The spectrum of **2c** also shows a weak MLCT band with a comparable, if slightly lower, oscillator strength, which again occurs between a Re-based HOMO - 1 and the bipyridine ligand-based LUMO (Figure 6d, Figure S18). As for **1b**/**2b**, this transition is blue-shifted compared to that in **1c** due to the higher-energy LUMO (Figure S29). The strong shorter-wavelength feature in Figure 6d is a combination of three bands at 295, 284, and 280 nm. The longer-wavelength band at 295 nm was assigned as predominantly a $\pi \rightarrow \pi^*$ transition based on the NTOs but with some MLCT character (Figure S19), the latter of which may explain its ∼3× smaller oscillator strength than the corresponding $\pi \rightarrow \pi^*$ transition in **1c**, relative to the smaller ∼2× difference in oscillator strengths of the electronic transitions in **1b**/**2b** (cf. Table 5). This reduction in oscillator strength can also be seen in the measured spectra in Figure 3. The two higher-energy transitions at 284 and 280 nm were assigned as predominantly MLCT, which is consistent with their weak oscillator strengths (Figures S20/S21).

The simulated spectrum of **M3** (Figure 6e) shows a major peak comprising a single bright state at 363 nm and a shoulder feature composed of two transitions at 335 and 327 nm. The long-wavelength transition mostly comprises a HOMO → LUMO excitation and was assigned as a $\pi \rightarrow \pi^*$ with some MLCT character from participation of the Pt d orbitals in the HOMO (Figure 9a). The ligand-based HOMO is therefore destabilized and raised above the equivalent Re-based orbitals that form the HOMO in **1c**. The extended conjugation in the HOMO due to incorporation into the diyne may also explain the enhanced oscillator strength of the transition relative to **1b** and **1c**. The two shoulder features can both be assigned, based on the NTOs, as MLCT transitions from the Re moiety (Figure 9b, Figures S23/24). The two prominent peaks in the spectrum of **M4** (Figure 6f) arise from three transitions at 331, 284, and 281 nm which, as for **M3**, can again be assigned as a long-wavelength $\pi \rightarrow \pi^*$ and two shorter-wavelength MLCT bands (Figures S25−27). All three are blue-shifted with respect

https://dx.doi.org/10.1021/acs.inorgchem.0c02747
Inorg. Chem. 2021, 60, 745−759

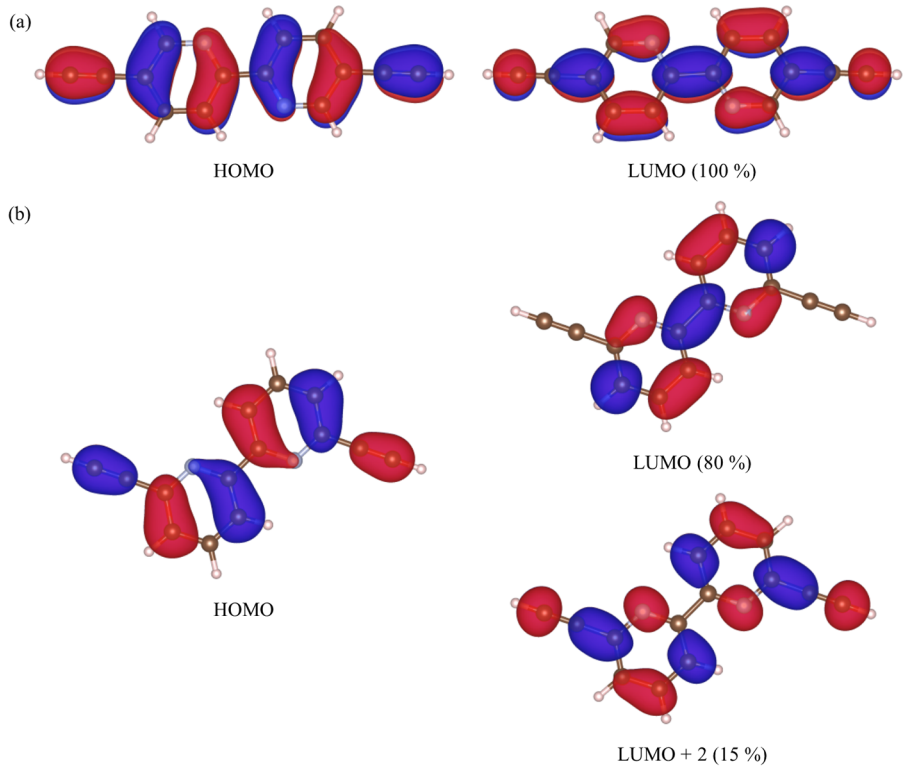

Figure 7. (a) Images of the highest-occupied and lowest-unoccupied molecular orbitals (HOMO/LUMO) in **1b**, which account for the bright $\pi \rightarrow \pi^*$ electronic excitation. (b) Images of the HOMO, LUMO, and LUMO+2 orbital in **2b** with the percentage contribution of the latter virtual orbitals to the electronic transition as marked. The isosurfaces are drawn to a contour value of 2.5×10^{-2} e bohr^{-3}.

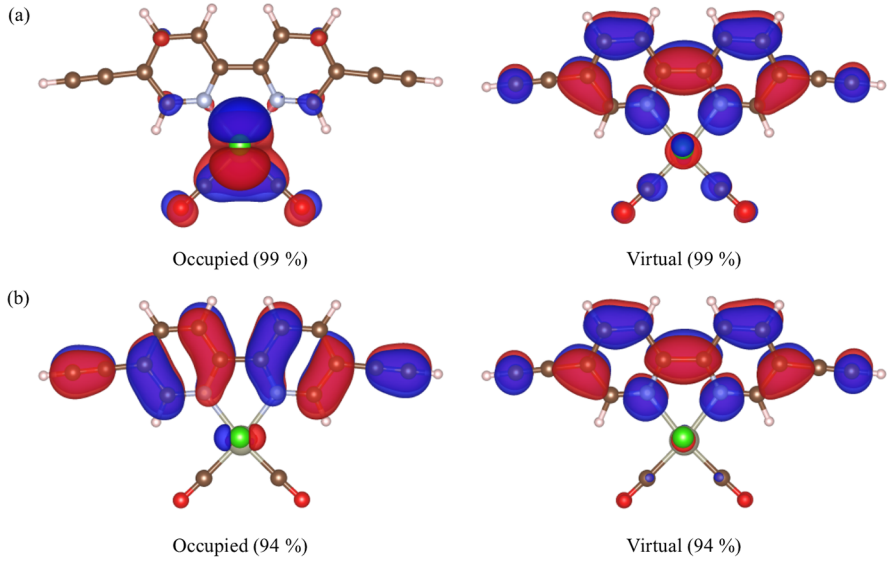

Figure 8. Occupied particle and virtual hole states obtained from natural transition orbitals (NTOs) analyses[46] of the dominant optical absorptions of **1c** at 355 (a) and 305 nm (b) identified in Figure 6/Table 5. The isosurfaces are drawn to a contour value of 2.5×10^{-2} e bohr^{-3}.

to the corresponding transitions in **M3**, which can be ascribed to the destabilization of the LUMO as seen in the **1b**/**2b** and **1c**/**2c** pairs (Figures S28–S30).

The low-lying triplet states in **1b** and **2b** were assigned based on the NTOs as $\pi \rightarrow \pi^*$ excitations (Table 6; Figures S31–S36). The lowest-lying triplet excitation in **1c** is predicted to occur at 492 nm and was also characterized as a $\pi \rightarrow \pi^*$ (Figure S37), whereas the next-highest triplet excitations at 391 and 377 nm are primarily MLCT bands (Figures S38/S39). In **2c**, on the other hand, the lowest-lying triplet states at 443 and 402 nm are of mixed MLCT and $\pi \rightarrow \pi^*$ character (Figures S40/S41), while the higher-lying state at 374 nm is predominantly an MLCT excitation (Figure S42). The simulated spectrum of **M3** in Figure 6e shows two triplet states below the bright, long-wavelength singlet excitation, which were both characterized as a $\pi \rightarrow \pi^*$ transitions (Figures S43/S44). In **M4**, there are three triplet states at notably longer wavelengths than the absorption onset, and these were again characterized as $\pi \rightarrow \pi^*$ transitions (Figures S45–S47). The change in the nature of the triplet states on going from the

https://dx.doi.org/10.1021/acs.inorgchem.0c02747
Inorg. Chem. 2021, 60, 745–759

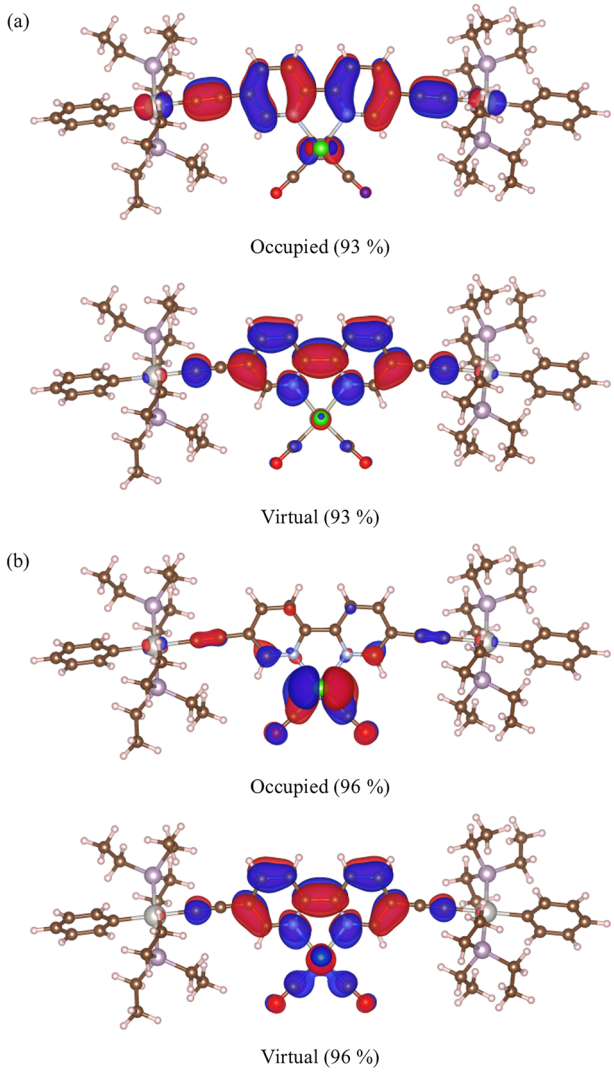

Figure 9. Occupied particle and virtual hole states obtained from natural transition orbitals (NTOs) analyses[46] of the optical absorptions of **M3** at 363 (a) and 335 nm (b) identified in Figure 6/Table 5. The NTOs associated with the second MLCT transition at 327 nm are substantially similar to those in (b) and are therefore not shown (cf. Figure S24). The isosurfaces are drawn to a contour value of 2.5×10^{-2} e bohr^{-3}.

chelated spacers to the heterobimetallic diynes is consistent with the shortening of the MLCT state lifetime and lengthening of the π^* lifetime observed in the picosecond-nanosecond dynamics measurements (cf. Table 4). The mixed character of the triplet states in the 6,6′-bipyridine species may also explain the larger contribution of the longer-lived $\pi \rightarrow \pi^*$ states to the transients in Figure 5.

In summary, for the 5,5′-bipyridine series, these electronic-structure calculations show that chelation of the bipyridine spacer ligand **1b** with $Re(CO)_3Cl$ in **1c** leads to a red shift of the optically bright $\pi \rightarrow \pi^*$ electronic transition in **1b** and introduces a weaker low-lying MLCT band. Subsequent incorporation of the chelated bipyridine into the Pt(II) diyne **M3** destabilizes the highest-lying bipyridine-based orbital, red shifts the $\pi \rightarrow \pi^*$ transition to lower energy than the Re-bipyridine MLCT state in **1c** and enhances its oscillator strength, and also red shifts and enhances the MLCT state in the chelated spacer precursor. The destabilization of the HOMO and red shift of the $\pi \rightarrow \pi^*$ transition represents an interesting effect of incorporating the spacer into the diyne. The higher energy and lower oscillator strength of the $\pi \rightarrow \pi^*$ transition in the 6,6′-bipyridine ligand **2b** can be ascribed to destabilization of the LUMO and poorer spatial overlap with the HOMO resulting in higher-energy virtual orbitals being involved in the transition. This highlights the sensitivity of the optical properties to the topology of the bipyridine spacer group, as observed in the absorption and emission measurements. As for **1b**, chelation of **2b** with $Re(CO)_3Cl$ introduces a weak low-lying MLCT band but also introduces some MLCT character into the higher-energy $\pi \rightarrow \pi^*$ transition, which may again serve to reduce its oscillator strength. The Pt(II) diyne **M4** shows similar spectral features to **M3**, with the destabilization of the bipyridine-based LUMO in the former resulting in a general predicted blue shift of the electronic transitions. Finally, analysis of the spin-forbidden triplet excitations also shows that the spacer topology, the chelation of the spacer with Re(I), and the incorporation of the chelated spacers into Pt(II) diynes have a substantial effect on the nature of the emissive states.

CONCLUSIONS

We have synthesized and characterized two Re(I)-coordinated diterminal alkynyl ligands, *viz.*, $Re(CO)_3Cl$-5,5′-diethynyl-2,2′-bipyridine and $Re(CO)_3Cl$-6,6′-diethynyl-2,2′-bipyridine, which we have subsequently incorporated as spacer groups into Pt(II) diynes and polyynes. Structural characterization of a Pt(II) diyne model complex reveals π stacking and a variety of weak intermolecular/interchain interactions in the solid state. As evidenced by optical absorption and emission spectroscopy and computational modeling, the photophysical properties of the Pt(II) diynes and polyynes show a high sensitivity to the topology of the bipyridine spacer group. Optical spectroscopy shows that chelation of the bipyridine ligands produces a red shift in the $\pi \rightarrow \pi^*$ transition and introduces weak, long-wavelength MLCT bands, both of which are further red-shifted in the Pt(II) diynes and polyynes. The metalated species appear to show aggregation in a solution, leading to substantial enhancement of the extinction coefficient with concentration. Emission spectroscopy reveals prominent blue/green emission associated with the Re(I) chromophore in the chelated bipyridines and Pt(II) diynes, whereas the Pt(II) polyynes only show shorter-wavelength bipyridine-centered emission. Picosecond-nanosecond dynamics measurements identify short-lived MLCT excited states and 1−2 long-lived π^* states in the chelated spacers, and incorporation of the spacers into the model Pt(II) diynes suppresses the MLCT state and significantly shortens its lifetime. Computational modeling confirmed the higher energetic stability of the 5,5′-bipyridine species compared to the 6,6′-bipyrdine analogues and allowed us to establish the nature of the brightest electronic transitions and low-lying triplet states in the optical absorption spectra. These calculations also reveal a remarkable destabilization of the bipyridine-based π orbital in the model diynes due to interaction with the Pt d orbitals, which results in the optically bright $\pi \rightarrow \pi^*$ transitions being lowered in energy compared to the long-wavelength Re $d\pi \rightarrow \pi^*$ MLCT transition in the chelated spacer precursors. In summary, our systematic studies have elucidated the effect of introducing a second metal ion into rigid-rod Pt(II) polyynes by chelation of the main-chain spacer groups and thus highlighted the potential utility of this

https://dx.doi.org/10.1021/acs.inorgchem.0c02747
Inorg. Chem. 2021, 60, 745−759

strategy for fine-tuning the optoelectronic properties of these materials for future technological applications.

EXPERIMENTAL SECTION

General Procedures. All reactions were performed in a dry argon atmosphere using standard Schlenk techniques. Solvents were distilled and predried before being used according to standard procedures.[42] Unless stated otherwise, all chemicals were obtained from Sigma-Aldrich and used without further purification. *trans*-[Pt(Ph)Cl-$(PEt_3)_2$] and *trans*-[$(P^nBu_3)_2PtCl_2$] were prepared following reported procedures.[43,44] Column chromatography was performed using either Kieselgel 60 (70−230) silica gel or Brockman grade II−III alumina. NMR spectra were recorded on Bruker MM-250 and WM-400 spectrometers in $CDCl_3$. ^1H and ^{13}C NMR spectra were referenced to solvent resonances and ^{31}P NMR spectra were referenced to an external phosphoric acid standard (85% H_3PO_4). Mass spectra were acquired using a Kratos MS 890 spectrometer using electrospray ionization (ESI). CH_2Cl_2 solutions of the ligand precursors, diynes, and polyynes were prepared at concentrations of 10^{-5}−10^{-4} M. IR spectra of 10^{-4} M solutions were recorded using a Cary 630 FT-IR spectrometer. Absorption spectra were recorded at solution concentrations of 1×10^{-5}−3×10^{-5} M on a Varian-Cary 50 UV−visible spectrophotometer in a 1 cm quartz cuvette. Solution emission spectra were recorded from 10^{-5} M solutions using a Shimadzu RF-5301 PC spectrofluorophotometer. Solid-state emission spectra were recorded using a PerkinElmer LS 55 fluorescence spectrometer. Lifetime measurements were performed using the time-correlated single photon counting (TCSPC) setup described elsewhere.[47] Microanalyses were performed using a PerkinElmer 2400 Series II CHNS/O elemental analyzer. Molar masses of the Pt(II) polyynes were determined by gel-permeation chromatography/light-scattering (GPC/LS) analysis. GPC was carried out using two PL Gel 30 cm, 5 μm mixed C columns at 30 °C running in THF at 1 mL min^{-1} with a Roth Model 200 high-precision pump. This was coupled to a DAWN DSP Wyatt Technology multiangle laser light-scattering (MALLS) apparatus with 18 detectors and auxiliary Viscotek Model 200 differential refractometer/viscometers, which were used to calculate the molecular weights.

Synthesis and Characterization of Precursors, Dimers, and Polymers. The precursors (**1a**, **1b**, **2a**, and **2b**), dimers (**M1** and **M2**), and polymers (**P1** and **P2**) were prepared and characterized according to previously reported procedures.[30,31]

Rhenium(I) Tricarbonyl Chloride-5,5′-bis(ethynyl)-2,2′-bipyridine (1c). A mixture of **1b** (0.050 g, 0.24 mmol) with rhenium(I) pentacarbonyl chloride (0.18 g, 0.50 mmol) was dissolved in toluene (20 mL). The solution was stirred at 60 °C overnight. After cooling to room temperature, the solvent was removed under reduced pressure. The mixture was purified by passing it through an alumina column using hexane/CH_2Cl_2 (1:2) as the eluent, and further purification by preparative alumina thin layer chromatography yielded **1c** as an orange solid (0.064 g, 0.13 mmol, 49% yield, decomposition temp. 250 °C). IR (CH_2Cl_2): ν/cm^{-1} 1896, 1905, 2015 (C═O), 2120 (C≡C), 3296 (C≡CH). ^1H NMR (250 MHz, $CDCl_3$): δ/ppm 9.11 (dd, J = 2.0, 0.78 Hz, 2H, $H_{6,6'}$), 8.13 (d, J = 7.9 Hz, 2H, $H_{3,3'}$), 8.11 (dd, J = 8.1, 2.0 Hz, 2H, $H_{4,4'}$), 3.50 (s, 2H, C≡C−H). ^{13}C NMR (100 MHz, $CDCl_3$): δ/ppm 155.32 ($C_{2,2'}$), 149.64 ($C_{6,6'}$), 137.75 ($C_{3,3'}$), 124.66 ($C_{4,4'}$), 119.30 ($C_{5,5'}$), 88.46, 79.90 (C≡C). ESI-MS: m/z 511 $[M + 2]^+$. Anal. calc. for $C_{17}H_8N_2O_3ClRe$: C - 38.81; H - 2.16; N - 5.28%, found: C - 38.78; H - 2.15; N - 5.25%.

Rhenium(I) Tricarbonyl Chloride-6,6′-bis(ethynyl)-2,2′-bipyridine (2c). Similar procedures to those used to obtain **1c** were followed starting from **2b** (0.13 g, 0.63 mmol). **2c** was obtained as an orange solid after purification (0.080 g, 0.39 mmol, 62% yield; decomposition temp. 149 °C). IR (CH_2Cl_2): ν/cm^{-1} 1853, 1907, 2017 (C═O), 2115(C≡C), 3291 (C≡CH). ^1H NMR (250 MHz $CDCl_3$): δ/ppm 8.11 (d, 2H, J = 7.6 Hz, $H_{3,3'}$), 7.82 (t, J = 7.9 Hz, 2H, $H_{4,4'}$), 7.54 (d, J = 7.7 Hz, 2H, $H_{5,5'}$), 3.9 (s, 2H, C≡NC−H). ^{13}C NMR (100 MHz, $CDCl_3$): δ/ppm 157.41 ($C_{2,2'}$), 146.12 ($C_{6,6'}$), 138.53 ($C_{3,3'}$), 130.71 ($C_{4,4'}$), 122.68 ($C_{5,5'}$), 89.75, 81.70 (C≡C). ESI-MS: m/z 516 $[M]^+$. Anal. calc. for $C_{17}H_8N_2O_3ClRe$: C - 38.81; H - 2.16; N - 5.28%, found: C - 38.79; H - 2.14; N - 5.26%.

***trans*-[(Ph)$(Et_3P)_2$Pt−C≡C−R−C≡C−Pt-$(PEt_3)_2$(Ph)] (R = $(CO)_3$ClRe(I)-2,2′-bipyridine-5,5′-diyl) (M3).** To a stirred solution of *trans*-[$(PEt_3)_2$(Ph)PtCl] (0.85 g, 0.16 mmol) and **1c** (0.40 g, 0. 78 mmol) in CH_2Cl_2/$^iPr_2NH$ (50 mL 1:1 v/v) under argon was added a catalytic amount (~5 mg, 0.0026 mmol) of CuI. The yellow solution was stirred at room temperature for 15 h, after which all volatile components were removed under reduced pressure. The residue was dissolved in CH_2Cl_2 and passed through a silica column eluting with hexane/CH_2Cl_2 (1:1, v/v). Removal of the solvents under vacuum gave the title complex as a yellow/orange solid (0.044 g, 0.029 mmol, 40% yield, decomposition temperature 198.5 °C). IR (CH_2Cl_2): ν/cm^{-1} 1885, 1909, 2016 (C═O), 2085(C≡C). ^1H NMR (250 MHz, $CDCl_3$): δ/ppm 8.82 (s, 2H, $H_{6,6}$), 7.76 (dd, J = 6.9, 1.6 Hz, 2H, $H_{3,3}$), 7.41 (s, 2H, $H_{4,4}$), 7.26 (d, J = 7.2, 4H, H_{ortho}Ph), 6.94 (t, J = 7.6 Hz, 4H, H_{meta} Ph), 6.83 (t, J = 7.5 Hz, 2H, H_{para} Ph), 1.75 (m, 24H, PCH_2), 1.12 (t, 36H, J = 6.4 Hz, $P(CH_2CH_3)$). ^{13}C NMR (100 MHz, $CDCl_3$): δ/ppm 150.47 ($C_{2,2}$), 144.22 ($C_{6,6}$), 138.86($C_{3,3}$), 127.1 (C Ph), 121.2 ($C_{4,4}$), 115.3 ($C_{5,5}$), 110.4 (C≡C), 15.09 ($P(CH_2CH_3)$), 8.05 (CH_3). $^{31}P\{^1H\}$ NMR (162 MHz, $CDCl_3$): δ 10.02 ($^1J_{Pt-P}$ = 2649.47 Hz). ESI-MS: m/z 1525 $[M]^+$. Anal. calc. for $C_{53}H_{76}N_2O_3P_4Pt_2ReCl$: C - 41.74; H - 5.02; N - 1.84%, found: C - 41.23; H - 5.27; N - 1.98%.

***trans*-[(Ph)$(Et_3P)_2$Pt−C≡C−R−C≡C−Pt−$(PEt_3)_2$(Ph)](R = $(CO)_3$ClRe-6,6′-bis(ethynyl)-2,2′-bipyridine) (M4).** **M4** was prepared following a similar procedure as for **M3** starting from *trans*-[$(PEt_3)_2$(Ph)PtCl] (0.079 g, 0.15 mmol) and **2c** (0.037 g, 0.073 mmol). A yellow solid was obtained after purification (0.050 g, 0.033 mmol, 45%; decomposition temp. 255.5 °C). IR (CH_2Cl_2): ν/cm^{-1} 1875, 1910, 2013 (C═O), 2066 (C≡C). ^1H NMR (250 MHz, $CDCl_3$): δ/ppm 7.73 (d, J = 7.7 Hz, 2H, $H_{5,5}$), 7.63 (t, J = 7.9 Hz, 2H, $H_{3,3}$), 7.42 (dd, J = 7.9, 2.0 Hz, 2H, $H_{4,4}$), 7.32 (d, J = 7.5 Hz, 4H, H_{ortho}Ph), 7.05 (t, J = 7.7 Hz, 4H, H_{meta} Ph), 6.84 (t, J = 7.3 Hz, 2H, H_{para} Ph), 1.75 (m, 24H, PCH_2), 1.10 (m, 36H, $P(CH_2CH_3)$. ^{13}C NMR (100 MHz, $CDCl_3$): δ/ppm 156.88 ($C_{2,2}$), 151.15 ($C_{6,6}$), 136.07 ($C_{3,3}$), 130.89−127.80 (C Ph), 121.43 ($C_{4,4}$), 117.75 ($C_{5,5}$), 112.66 (C≡C), 15.09 (PCH_2CH_3), 7.97 (CH_3). $^{31}P\{^1H\}$ NMR (162 MHz, $CDCl_3$): δ 9.92 ($^1J_{Pt-P}$ = 2650.25 Hz). ESI-MS: m/z 1528 $[M + 4]^+$. Anal. calc. for $C_{53}H_{76}N_2O_3P_4Pt_2ReCl$: C - 41.74; H - 5.02; N - 1.84%, found: C - 41.89; H - 5.19; N - 1.90%.

***trans*-[$(^nBu_3P)_2$Pt−C≡C−R−C≡C−]$_n$ (R = Re(CO)$_3$Cl-2,2′-bipyridine-5,5′-diyl) (P3).** CuI (0.015 g, 0.079 mmol) was added to a mixture of *trans*-[$Pt(P^nBu_3)_2Cl_2$] (0.040 g, 0.0060 mmol) and **1c** (0.030 g, 0.0060 mmol) in $^iPr_2NH/CH_2Cl_2$ (50 mL, 1:1 v/v). The solution was stirred at room temperature for 15 h, after which all volatile components were removed under reduced pressure. The residue was dissolved in CH_2Cl_2 and purified through a short alumina column. After removal of the solvent under reduced pressure, a yellow film was obtained and then washed with methanol to give **P3** (0.0054 g, 82% yield). Further purification could be performed by precipitation from CH_2Cl_2 in MeOH. IR (CH_2Cl_2): ν/cm^{-1} 1897, 1920, 2018 (C═O), 2089 (C≡C). ^1H NMR (250 MHz, $CDCl_3$): δ/ppm 7.94 (d, 2H, J = 7.0 Hz, $H_{3,3'}$), 7.17 (t, 2H, J = 7.0 Hz, $H_{4,4'}$), 6.86 (d, 2H, J = 7.6 Hz, $H_{5,5'}$), 2.11 (m, 12H, $PCH_2(CH_2)_2(CH_3)$), 1.49 (m, 12H, $PCH_2(CH_2)_2(CH_3)$), 1.41 (m, 12H, $PCH_2(CH_2)_2(CH_3)$), 0.92 (t, J = 7.2 Hz, 18H, $P(CH_2)_3CH_3$)). ^{13}C NMR (100 MHz, $CDCl_3$): δ/ppm 156.72 ($C_{2,2'}$), 145.28 ($C_{6,6'}$), 136.27 ($C_{3,3'}$), 126.15 ($C_{4,4'}$), 122.10 ($C_{5,5'}$), 115.98, 109.32 (C≡C), 29.72−23.18 ($PCH_2CH_2CH_2CH_3$), 14.35 (CH_3). $^{31}P\{^1H\}$ NMR (162 MHz, $CDCl_3$): δ/ppm 3.29 ($^1J_{Pt-P}$ = 2340.25 Hz). Anal. calc. for $(C_{41}H_{60}N_2P_2O_3ClRePt)_n$: C - 44.47; H - 5.46; N - 2.53%, found: C - 44.61; H - 5.51; N - 2.59%. GPC (THF): M_n = 61,000 g mol^{-1} (n = 55), M_w = 77,000 g mol^{-1}, polydispersity index = 1.26.

***trans*-[$(^nBu_3P)_2$Pt−C≡C−R−C≡C−]$_n$ (R = Re(CO)$_3$Cl-2,2′-bipyridine-6,6′-diyl) (P4).** **P4** was prepared as described above for **P3** starting from *trans*-[$Pt(P^nBu_3)_2Cl_2$] (0.040 g, 0.0060 mmol) and **2c** (0.030 g, 0.0060 mmol) in CH_2Cl_2/$^iPr_2NH$ (40 mL, 1:1, v/v) with catalytic CuI (0.011 g, 0.0058 mmol). After purification, the product was obtained as a bright yellow solid (0.0046 g, 70% yield,

https://dx.doi.org/10.1021/acs.inorgchem.0c02747
Inorg. Chem. 2021, 60, 745−759

decomposition temp. 256 °C). IR (CH_2Cl_2): ν/cm^{-1} 1871, 1911, 2012 cm^{-1} (C═O) 2068 cm^{-1}(C≡C). ^{1}H NMR (250 MHz, $CDCl_3$): δ/ppm 8.10 (m, 2H, $H_{3,3'}$), 7.32 (t, 2H, J = 7.2 Hz, $H_{4,4'}$), 6.24 (d, 2H, J = 7.0 Hz, $H_{5,5'}$), 1.56 (m, 14H, $PCH_2(CH_2)_2(CH_3)$), 1.47−1.29 (m, 22H, $PCH_2(CH_2)_2(CH_3)$), 0.88 (t, J = 7.0 Hz, 18H, $P(CH_2)_3CH_3$). ^{13}C NMR (100 MHz, $CDCl_3$): δ/ppm 156.23 ($C_{2,2'}$), 145.21 ($C_{6,6'}$), 136.32 ($C_{3,3'}$), 126.08 ($C_{4,4'}$), 120.79 ($C_{5,5'}$), 115.32, 112.54 (C≡C), 30.13−23.68 ($PCH_2CH_2CH_2CH_3$), 14.37 (CH_3). ^{31}P{^{1}H} NMR (162 MHz, $CDCl_3$): δ/ppm 3.32 ($^1J_{Pt-P}$ = 2339.18). Anal. calc. for $(C_{41}H_{60}N_2P_2O_3ClRePt)_n$: C - 44.47; H - 5.46; N - 2.53%, found: C - 44.55; H - 5.50; N - 2.56%. GPC (THF): M_n = 55,000 g mol^{-1} (n = 50), M_w = 83,000 g mol^{-1}, PDI = 1.51.

X-ray Crystallography. Single-crystal X-ray diffraction experiments were performed at 150 K on a STOE IPDS (II) diffractometer using monochromatic Mo−K_α radiation (λ = 0.71073 Å) with the sample temperature controlled using an Oxford Diffraction Cryojet. The X-Area software was used for data collection and indexing. The structure was solved and refined using full-matrix least-squares on F^2 in SHELX2014[45] from the WinGX suite.[48] A multiscan absorption correction was applied. There was extensive disorder in the alkyl groups of the phosphine ligands, which were modeled over two or three sites using partial occupancies, constrained to sum to unity, and with additional constraints placed on the bond parameters to maintain reasonable bond lengths and angles. With the exception of some of the disordered carbon atoms in the alkyl chains of the phosphine ligands, all non-hydrogen atoms were refined anisotropically. Hydrogen atoms were included using rigid methyl groups or a riding model, with partial occupancies used as appropriate. Refinement was continued until convergence, and in the final cycles of refinement, a weighting scheme was used that gave a relatively flat analysis of variance.

Time-Resolved Fluorescence. Lifetime measurements were performed using time-correlated single photon counting (TCSPC). The TCSPC setup, described elsewhere,[47] is part of an ultrafast spectrometer (Halcyone, Ultrafast Systems, LLC) used to measure femtosecond fluorescence upconversion. Briefly, an excitation is obtained using a regenerative amplified Ti:sapphire laser (Libra, Coherent), which generates compressed laser pulses centered on 800 nm with a 70 fs fwhm, 4.26 W power, and a 5 kHz repetition rate. 90% of the output pulse is used to pump a Coherent OPerA Solo optical parametric amplifier (Light Conversion Ltd.) to generate spectrally tunable light from 240−2600 nm. For the current measurements, the OperA was adjusted at 350 and 380 nm (∼20 nJ) and used as the excitation beam after passing through a depolarizer to cancel any contributions from rotational dynamics (DPU-25, Thorlabs). A photomultiplier tube with an instrument response function (IRF) of ∼250 ps, measured from scattered excitation light, was used as the detector. Fluorescence was attenuated and directed to the detector, and a monochromator was used to adjust the detection wavelength. Decays were recorded to ∼10,000 counts in the peak channel. The decay transients were fitted to multiexponential functions convolved with the IRF.

Computational Modeling. Molecular quantum-chemical calculations were carried out using the density-functional theory (DFT) formalism as implemented in the Gaussian09 software.[49] The CAM-B3LYP hybrid functional[50] was used in conjunction with Pople split-valence basis sets[51] of 6-31g and 6-31g** quality for the H and non-H atoms, respectively. The LANL2DZ pseudopotential[52] and corresponding double-ζ basis sets were used to describe the Pt and Re atoms. Initial models of **1b**/**2b**, **1c**/**2c**, and **M3**/**M4** were prepared from X-ray structures or using the Avogadro software.[53] The molecular structures were optimized in the gas phase, and the minima were confirmed to be stationary points from the absence of imaginary modes in the vibrational Hessian matrix. Time-dependent DFT (TD-DFT) calculations were carried out on the optimized models using adiabatic B3LYP to identify the 50 lowest-energy singlet and triplet states, a subset of which were characterized using natural transition orbitals.[41] Visualization of the frontier orbitals was performed using VESTA.[54]

■ ASSOCIATED CONTENT

Supporting Information

The Supporting Information is available free of charge at https://pubs.acs.org/doi/10.1021/acs.inorgchem.0c02747.

> Crystallographic data for **1c** and **M4**; additional spectroscopic data; images and Cartesian coordinates of the optimized structures of **1b**, **2b**, **1c**, **2c**, **M3**, and **M4**; and characterization of optical transitions identified from TD-DFT calculations on **1b**, **2b**, **1c**, **2c**, **M3**, and **M4** including breakdowns into orbital components, images of NTOs, and orbital energy-level spectra (PDF)

Accession Codes

CCDC 1964156 and 2009579 contain the supplementary crystallographic data for this paper. These data can be obtained free of charge via www.ccdc.cam.ac.uk/data_request/cif, or by emailing data_request@ccdc.cam.ac.uk, or by contacting The Cambridge Crystallographic Data Centre, 12 Union Road, Cambridge CB2 1EZ, U.K. (fax: +44 1223 336033).

■ AUTHOR INFORMATION

Corresponding Authors

Muhammad S. Khan − *Department of Chemistry, Sultan Qaboos University, Al Khod 123, Sultanate of Oman*; Email: msk@squ.edu.om

Paul R. Raithby − *Department of Chemistry, University of Bath, Bath BA2 7AY, U.K.*; orcid.org/0000-0002-2944-0662; Email: p.r.raithby@bath.ac.uk

Jonathan M. Skelton − *Department of Chemistry, University of Bath, Bath BA2 7AY, U.K.; Department of Chemistry, University of Manchester, Manchester M13 9PL, U.K.*; orcid.org/0000-0002-0395-1202; Email: jonathan.skelton@manchester.ac.uk

Osama K. Abou-Zied − *Department of Chemistry, Sultan Qaboos University, Al Khod 123, Sultanate of Oman*; orcid.org/0000-0003-0497-8412; Email: abouzied@squ.edu.om

Authors

Ashanul Haque − *Department of Chemistry, College of Science, University of Ha'il, Ha'il 81451, Kingdom of Saudi Arabia; Department of Chemistry, Sultan Qaboos University, Al Khod 123, Sultanate of Oman*; orcid.org/0000-0002-6780-632X

Rayya Al-Balushi − *Department of Basic Sciences, College of Applied and Health Sciences, A'Sharqiyah University, Ibra 400, Sultanate of Oman*; orcid.org/0000-0002-5665-5175

Idris Juma Al-Busaidi − *Department of Chemistry, Sultan Qaboos University, Al Khod 123, Sultanate of Oman*

Nawal K. Al-Rasbi − *Department of Chemistry, Sultan Qaboos University, Al Khod 123, Sultanate of Oman*

Sumayya Al-Bahri − *Department of Chemistry, Sultan Qaboos University, Al Khod 123, Sultanate of Oman*

Mohammed K. Al-Suti − *Department of Chemistry, Sultan Qaboos University, Al Khod 123, Sultanate of Oman*

Complete contact information is available at: https://pubs.acs.org/10.1021/acs.inorgchem.0c02747

Notes

The authors declare no competing financial interest.

https://dx.doi.org/10.1021/acs.inorgchem.0c02747
Inorg. Chem. 2021, 60, 745−759

■ ACKNOWLEDGMENTS

M.S.K. thanks The BP Oman (Grant: EG/SQU-BP/SCI/CHEM/19/01) and The Ministry of Higher Education (MoHE), Oman (Grant: RC/RG-SCI/CHEM/20/01) for funding. P.R.R. is grateful to the Engineering and Physical Sciences Research Council (UK) for support (EP/K004956/1). R.A.A. gratefully acknowledges The Research Council (TRC), Oman (Project No. BFP/RGP/EI/18/076) for funding and A'Sharqiyah University, Oman for a research grant (ASU-FSFR/CAS/FSHN-01/2019). J.M.S. is currently supported by a UK Research and Innovation Future Leaders Fellowship (MR/T043121/1) and is also grateful to the UK Engineering and Physical Sciences Research Council for funding (EP/K004956/1 and EP/P007821/1) and to the University of Manchester for the award of a Presidential Fellowship. The authors acknowledge Dr. Rashid Ilmi, Department of Chemistry, Sultan Qaboos University, Oman for helpful discussions.

■ REFERENCES

(1) Haque, A.; Al-Balushi, R. A.; Al-Busaidi, I. J.; Khan, M. S.; Raithby, P. R. Rise of conjugated poly-ynes and poly(metalla-ynes): From design through synthesis to structure-property relationships and applications. *Chem. Rev.* **2018**, *118*, 8474−8597.

(2) Haque, A.; Al-Balushi, R. A.; Khan, M. S. σ-Acetylide complexes for biomedical applications: Features, challenges and future directions. *J. Organomet. Chem.* **2019**, *897*, 95−106.

(3) Haque, A.; Al Balushi, R. A.; Al-Busaidi, I. J.; Ilmi, R.; Al Rasbi, N.; Jayapal, M.; Khan, M. S.; Raithby, P. R. Synthesis, optical spectroscopy, structural, and DFT studies on dimeric iodo-bridged copper(I) complexes. *J. Organomet. Chem.* **2019**, *892*, 75−82.

(4) Ho, C. L.; Yu, Z. Q.; Wong, W. Y. Multifunctional polymetallaynes: properties, functions and applications. *Chem. Soc. Rev.* **2016**, *45* (19), 5264−95.

(5) Cheng, Y. J.; Yang, S. H.; Hsu, C. S. Synthesis of conjugated polymers for organic solar cell applications. *Chem. Rev.* **2009**, *109*, 5868−5923.

(6) Bunz, U. H. Poly(aryleneethynylene)s: Syntheses, properties, structures, and applications. *Chem. Rev.* **2000**, *100*, 1605−1644.

(7) Nguyen, P.; Gomez-Elipe, P.; Manners, I. Organometallic polymers with transition metals in the main chain. *Chem. Rev.* **1999**, *99*, 1515−1548.

(8) Long, N. J.; Williams, C. K. Metal alkynyl sigma complexes: Synthesis and materials. *Angew. Chem., Int. Ed.* **2003**, *42*, 2586−2617.

(9) Wilson, J. S.; Köhler, A.; Friend, R. H.; Al-Suti, M. K.; Al-Mandhary, M. R. A.; Khan, M. S.; Raithby, P. R. Triplet states in a series of Pt-containing ethynylenes. *J. Chem. Phys.* **2000**, *113*, 7627−7634.

(10) Wong, W.-Y.; Ho, C.-L. Organometallic photovoltaics: A new and versatile approach for harvesting solar energy using conjugated polymetallaynes. *Acc. Chem. Res.* **2010**, *43*, 1246−1256.

(11) Wong, W. Y.; Harvey, P. D. Recent progress on the photonic properties of conjugated organometallic polymers built upon the trans-bis (para-ethynylbenzene) bis (phosphine) platinum (II) chromophore and related derivatives. *Macromol. Rapid Commun.* **2010**, *31*, 671−713.

(12) Wong, W.-Y. Challenges in organometallic research-Great opportunity for solar cells and OLEDs. *J. Organomet. Chem.* **2009**, *694* (17), 2644−2647.

(13) Wong, W.-Y.; Ho, C.-L. Di-, oligo-and polymetallaynes: Syntheses, photophysics, structures and applications. *Coord. Chem. Rev.* **2006**, *250*, 2627−2690.

(14) Khan, M. S.; Al-Suti, M. K.; Maharaja, J.; Haque, A.; Al-Balushi, R. A.; Raithby, P. R. Conjugated poly-ynes and poly (metalla-ynes) incorporating thiophene-based spacers for solar cell (SC) applications. *J. Organomet. Chem.* **2016**, *812*, 13−33.

(15) Yam, V. W.; Au, V. K.; Leung, S. Y. Light-emitting self-assembled materials based on d(8) and d(10) transition metal complexes. *Chem. Rev.* **2015**, *115* (15), 7589−728.

(16) Wei, K.; Gao, Z.; Liu, H.; Wu, X.; Wang, F.; Xu, H. Mechanical activation of platinum-acetylide complex for olefin hydrosilylation. *ACS Macro Lett.* **2017**, *6*, 1146−1150.

(17) Green, K. A.; Cifuentes, M. P.; Samoc, M.; Humphrey, M. G. Syntheses and NLO properties of metal alkynyl dendrimers. *Coord. Chem. Rev.* **2011**, *255*, 2025−2038.

(18) Lima, J. C.; Rodriguez, L. Applications of gold(I) alkynyl systems: a growing field to explore. *Chem. Soc. Rev.* **2011**, *40*, 5442−5456.

(19) Al-Busaidi, I. J.; Haque, A.; Al Rasbi, N. K.; Khan, M. S. Phenothiazine-based derivatives for optoelectronic applications: A review. *Synth. Met.* **2019**, *257*, 116189.

(20) Al-Balushi, R. A.; Haque, A.; Jayapal, M.; Al-Suti, M. K.; Husband, J.; Khan, M. S.; Koentjoro, O. F.; Molloy, K. C.; Skelton, J. M.; Raithby, P. R. Experimental and theoretical investigation for the level of conjugation in carbazole-based precursors and their mono-, di-, and polynuclear Pt (II) complexes. *Inorg. Chem.* **2016**, *55*, 6465−6480.

(21) Al-Balushi, R. A.; Haque, A.; Jayapal, M.; Al-Suti, M. K.; Husband, J.; Khan, M. S.; Skelton, J. M.; Molloy, K. C.; Raithby, P. R. Impact of the alkyne substitution pattern and metalation on the photoisomerization of azobenzene-based platinum(II) diynes and polyynes. *Inorg. Chem.* **2016**, *55*, 10955−10967.

(22) Shah, H. H.; Al-Balushi, R. A.; Al-Suti, M. K.; Khan, M. S.; Marken, F.; Sudlow, A. L.; Kociok-Kohn, G.; Woodall, C. H.; Raithby, P. R.; Molloy, K. C. New di-ferrocenyl-ethynylpyridinyl triphenyl-phosphine copper halide complexes and related di-ferricenyl electro-crystallized materials. *Dalton Trans.* **2014**, *43*, 9497−9507.

(23) Shah, H. H.; Al-Balushi, R. A.; Al-Suti, M. K.; Khan, M. S.; Woodall, C. H.; Sudlow, A. L.; Raithby, P. R.; Kociok-Kohn, G.; Molloy, K. C.; Marken, F. New multi-ferrocenyl- and multi-ferricenyl-materials via coordination-driven self-assembly and via charge-driven electro-crystallization. *Inorg. Chem.* **2013**, *52*, 12012−12022.

(24) Li, L.; Ho, C.-L.; Wong, W.-Y. Versatile control of the optical bandgap in heterobimetallic polymers through complexation of bithiazole-containing polyplatinynes with $ReCl(CO)_5$. *J. Organomet. Chem.* **2012**, *703*, 43−50.

(25) Wong, W.-Y.; Wong, W.-K.; Raithby, P. R. Synthesis, characterisation and properties of platinum (II) acetylide complexes of ferrocenylfluorene: Novel soluble donor-acceptor heterometallic materials. *J. Chem. Soc., Dalton Trans.* **1998**, No. 16, 2761−2766.

(26) Patil, A.; Heeger, A.; Wudl, F. Optical properties of conducting polymers. *Chem. Rev.* **1988**, *88* (1), 183−200.

(27) Brédas, J. L.; Silbey, R. *Conjugated polymers: the novel science and technology of highly conducting and nonlinear optically active materials*; Springer Science & Business Media: 2012; DOI: 10.1007/978-94-011-3476-7.

(28) Lee, C.; Yu, G.; Pakbaz, K.; Moses, D.; Sariciftci, N.; Wudl, F.; Heeger, A. Large enhancement of the transient and steady-state photoconductivity of conducting polymer/C60 composite films. *Synth. Met.* **1995**, *70* (1−3), 1353−1356.

(29) Yam, V. W.-W.; Lo, K. K.-W.; Wong, K. M.-C. Luminescent polynuclear metal acetylides. *J. Organomet. Chem.* **1999**, *578*, 3−30.

(30) Khan, M. S.; Al-Suti, M. K.; Ahrens, B.; Raithby, P. R.; Teat, S. J. Trans-(5,5′-Diethynyl-2, 2′-bipyridine) bis[phenylbis (triethylphosphine) platinum(II)]. *Acta Crystallogr., Sect. E: Struct. Rep. Online* **2004**, *60* (6), m735−m737.

(31) Khan, M. S.; Al-Mandhary, M. R. A.; Al-Suti, M. K.; Hisahm, A. K.; Raithby, P. R.; Ahrens, B.; Mahon, M. F.; Male, L.; Marseglia, E. A.; Tedesco, E.; Friend, R. H.; Kohler, A.; Feeder, N.; Teat, S. J. Structural characterisation of a series of acetylide-functionalised oligopyridines and the synthesis, characterisation and optical spectroscopy of platinum di-ynes and Ppoly-ynes containing oligopyridyl linker groups in the backbone. *Dalton Trans.* **2002**, *0*, 1358−1368.

(32) Gamelin, D. R.; George, M. W.; Glyn, P.; Grevels, F.-W.; Johnson, F. P. A.; Klotzbuecher, W.; Morrison, S. L.; Russell, G.; Schaffner, K.; Turner, J. J. Structural investigation of the ground and excited states of $ClRe(CO)_3(4, 4'\text{-bipyridyl})_2$ using vibrational spectroscopy. *Inorg. Chem.* **1994**, *33*, 3246−3250.
(33) Rotundo, L.; Azzi, E.; Deagostino, A.; Garino, C.; Nencini, L.; Priola, E.; Quagliotto, P.; Rocca, R.; Gobetto, R.; Nervi, C. Electronic effects of substituents on *fac*-M(bpy-R)$(CO)_3$ (M = Mn, Re) complexes for homogeneous CO2 electroreduction. *Front. Chem.* **2019**, *7*, 417.
(34) Lewis, J.; Long, N. J.; Raithby, P. R.; Shields, G. P.; Wong, W.-Y.; Younus, M. Synthesis and characterisation of new acetylide-functionalised oligothiophenes and their dinuclear platinum complexes. *J. Chem. Soc., Dalton Trans.* **1997**, No. 22, 4283−4288.
(35) Yamamoto, Y.; Shiotsuka, M.; Onaka, S. Luminescent rhenium (I)-gold (I) hetero organometallics linked by ethynylphenanthrolines. *J. Organomet. Chem.* **2004**, *689*, 2905−2911.
(36) Schanze, K. S.; Macqueen, B. D.; Perkins, T. A.; Cabana, L. A. Studies of intramolecular electron and energy transfer using the *fac*-(diimine) $Re^1(CO)_3$ chromophore. *Coord. Chem. Rev.* **1993**, *122*, 63−89.
(37) Worl, L. A.; Duesing, R.; Chen, P.; Meyer, T. J. Photophysical properties of polypyridyl carbonyl complexes of rhenium (I). *J. Chem. Soc., Dalton Trans.* **1991**, 849−858.
(38) Wang, B.; Wasielewski, M. R. Design and synthesis of metal ion-recognition-induced conjugated polymers: an approach to metal ion sensory materials. *J. Am. Chem. Soc.* **1997**, *119*, 12−21.
(39) Sacksteder, L.; Lee, M.; Demas, J.; DeGraff, B. Long-lived, highly luminescent rhenium (I) complexes as molecular probes: intra- and intermolecular excited-state interactions. *J. Am. Chem. Soc.* **1993**, *115*, 8230−8238.
(40) Liu, Y.; Liu, H.; Yan, H.; Liu, Y.; Zhang, J.; Shan, W.; Lai, P.; Li, H.; Ren, L.; Li, Z. Aggregation-induced absorption enhancement for deep near-infrared II photoacoustic imaging of brain gliomas in vivo. *Adv. Sci.* **2019**, *6*, 1801615.
(41) Liu, Z.; Shao, P.; Huang, Z.; Liu, B.; Chen, T.; Qin, J. Two-photon absorption enhancement induced by aggregation due to intermolecular hydrogen bonding in V-shaped 2-hydroxypyrimidine derivatives. *Chem. Commun.* **2008**, No. 19, 2260−2262.
(42) Kumar, A.; Sun, S.-S.; Lees, A. J. In *Photophysics of Organometallics*; Springer: 2009; pp 37−71, DOI: 10.1007/3418_2009_2.
(43) Lees, A. J. Luminescence properties of organometallic complexes. *Chem. Rev.* **1987**, *87* (4), 711−743.
(44) Baková, R.; Chergui, M.; Daniel, C.; Vlček, A., Jr; ZáliŠ, S. Relativistic effects in spectroscopy and photophysics of heavy-metal complexes illustrated by spin-orbit calculations of [Re(imidazole)-$(CO)_3$ (phen)]$^+$. *Coord. Chem. Rev.* **2011**, *255* (7−8), 975−989.
(45) Zahid, N. I.; Ji, L.; Khyasudeen, M. F.; Friedrich, A.; Hashim, R.; Marder, T. B.; Abou-Zied, O. K. Evidence of increased hydrophobicity and dynamics inside the tail region of glycolipid self-assemblies using 2-n-alkyl-pyrene derivatives to probe different locations. *Langmuir* **2019**, *35*, 9584−9592.
(46) Martin, R. L. Natural transition orbitals. *J. Chem. Phys.* **2003**, *118*, 4775−4777.
(47) Zahid, N. I.; Mahmood, M. S.; Subramanian, B.; Mohd Said, S.; Abou-Zied, O. K. New insight into the origin of the red/near-infrared intense fluorescence of a crystalline 2-hydroxychalcone derivative: A comprehensive picture from the excited-state femtosecond dynamics. *J. Phys. Chem. Lett.* **2017**, *8* (22), 5603−5608.
(48) Farrugia, L. J. WinGX suite for small-molecule single-crystal crystallography. *J. Appl. Crystallogr.* **1999**, *32*, 837−838.
(49) Frisch, M.; Trucks, G.; Schlegel, H.; Scuseria, G.; Robb, M.; Cheeseman, J.; Scalmani, G.; Barone, V.; Petersson, G.; Nakatsuji, H. *Gaussian 09*, Revision E.01; Gaussian. Inc.: Wallingford CT, 2016.
(50) Becke, A. D. Density-functional thermochemistry. III. The role of exact exchange. *J. Chem. Phys.* **1993**, *98* (7), 5648−5652.
(51) Ditchfield, R.; Hehre, W. J.; Pople, J. A. Self-consistent molecular-orbital methods. IX. An extended Gaussian-type basis for molecular-orbital studies of organic molecules. *J. Chem. Phys.* **1971**, *54*, 724−728.
(52) Hay, P. J.; Wadt, W. R. Ab initio effective core potentials for molecular calculations. Potentials for the transition metal atoms Sc to Hg. *J. Chem. Phys.* **1985**, *82*, 270−283.
(53) Hanwell, M. D.; Curtis, D. E.; Lonie, D. C.; Vandermeersch, T.; Zurek, E.; Hutchison, G. R. Avogadro: an advanced semantic chemical editor, visualization, and analysis platform. *J. Cheminf.* **2012**, *4*, 17.
(54) Momma, K.; Izumi, F. VESTA 3 for three-dimensional visualization of crystal, volumetric and morphology data. *J. Appl. Crystallogr.* **2011**, *44* (6), 1272−1276.

https://dx.doi.org/10.1021/acs.inorgchem.0c02747
Inorg. Chem. 2021, 60, 745−759